

# Scaling Self-Supervised and Cross-Modal Pretraining for Volumetric CT Transformers

Cris Claessens<sup>\*,1</sup>

Christiaan Viviers<sup>\*,1</sup>

Fons van der Sommen<sup>1</sup>

Giacomo D'Amicantonio<sup>2</sup>

Egor Bondarev<sup>2</sup>

Dept. of Electrical Engineering, Eindhoven University of Technology, Eindhoven, The Netherlands

<sup>1</sup>ARIA Lab, <sup>2</sup>AIMS Lab, <sup>\*</sup>Contributed equally

{c.h.b.claessens, c.g.a.viviers, g.d.amicantonio, e.bondarev, fvdsommen}@tue.nl

## Abstract

We introduce *SPECTRE*, a fully transformer-based foundation model for volumetric computed tomography (CT). Our *Self-Supervised & Cross-Modal Pretraining for CT Representation Extraction (SPECTRE)* approach utilizes scalable 3D Vision Transformer architectures and modern self-supervised and vision–language pretraining strategies to learn general-purpose CT representations. Volumetric CT poses unique challenges, such as extreme token scaling, geometric anisotropy, and weak or noisy clinical supervision, that make standard transformer and contrastive learning recipes ineffective out of the box. The framework jointly optimizes a local transformer for high-resolution volumetric feature extraction and a global transformer for whole-scan context modeling, making large-scale 3D attention computationally tractable. Notably, *SPECTRE* is trained exclusively on openly available CT datasets, demonstrating that high-performing, generalizable representations can be achieved without relying on private data. Pretraining combines DINO-style self-distillation with SigLIP-based vision–language alignment using paired radiology reports, yielding features that are both geometrically consistent and clinically meaningful. Across multiple CT benchmarks, *SPECTRE* consistently outperforms prior CT foundation models in both zero-shot and fine-tuned settings, establishing *SPECTRE* as a scalable, open, and fully transformer-based foundation model for 3D medical imaging.<sup>1</sup>

## 1. Introduction

Self-supervised learning (SSL) and vision-language alignment (VLA) are two rapidly maturing paradigms for learning high-quality visual representations in computer vision. SSL comprises methods that construct surrogate objectives from unlabeled images so that models learn invariances

<sup>1</sup>Code available at: <https://github.com/cclaess/SPECTRE>

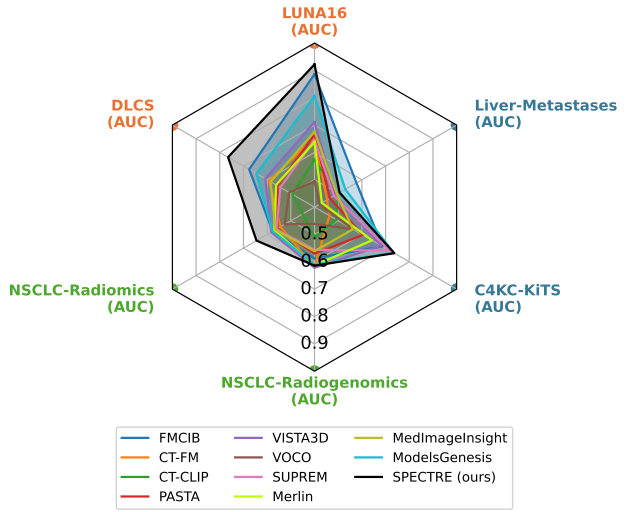


Figure 1. Radar plot comparing 11 CT foundation models across six biomarker classification benchmarks using frozen-embedding kNN classifiers. Diagnostic tasks on chest CT are shown in orange, prognostic tasks on chest CT in green, and prognostic tasks on abdominal CT in blue. *SPECTRE* achieves the highest performance on four of the six benchmarks, demonstrating stronger and more transferable volumetric representations compared to prior models.

and mid-level features without any text or structured labels [11, 20]. In contrast, VLA directly couples visual encoders with textual encoders through alignment objectives so that learned features carry high-level compositional semantics grounded in language [48]. These two families of objectives address different statistical problems: SSL provides dense, data-efficient priors about image structure, while VLA injects explicit semantic grounding that is essential for many downstream retrieval and reasoning tasks.

Several recent works have adapted elements of SSL and VLA to 2D medical imaging, yielding foundation mod-

els that transfer well across different downstream tasks [5, 8, 10, 31]. However, these successes do not automatically translate to volumetric clinical imaging, such as computed tomography (CT). One reason is architectural: Vision Transformers (ViTs) are the backbone of many modern foundation models because they provide a flexible, scalable attention mechanism with minimal hand-crafted inductive bias [15]. In natural images, that flexibility is an advantage when large, diverse datasets and expressive pretraining objectives are available. In medical imaging, and especially in volumetric modalities, the absence of strong intrinsic locality and translational biases has historically slowed transformer adoption: in low-data or heterogeneous-data regimes, these priors act as regularizers that improve sample efficiency and robustness [16]. In the context of CT imaging, these geometrical and local priors need to be introduced in the model by design, through tokenization, positional encodings, attention design, or auxiliary objectives rather than rely on these biases to be present by default.

Volumetric CT shifts the technical problem in several fundamental ways that interact directly with both architecture and objective choice. First, naive patching of 3D volumes produces token counts that scale roughly cubically with resolution, and transformer self-attention scales quadratically in token number [33]. Some of the most effective design choices in transformers at scale, such as global attention or large training batches, require a certain degree of approximation to be employed for CT imaging. Second, CT commonly exhibits strong geometric heterogeneity: anisotropic voxel spacing, variable field-of-view (FOV), and scanner-specific preprocessing (reconstruction kernels, denoising, dose modulation). Positional encodings and receptive field parameterizations that assume isotropy or simple translation invariance will therefore misrepresent interscan geometry. Hence, models must explicitly represent voxel spacing and slice sampling or learn geometry-aware receptive fields to generalize across protocols [19]. Third, clinical supervision is typically weak, noisy, and hierarchical (free-text reports, sparse tags, study-level labels), creating a tension between dense objectives that teach spatial precision (masked modeling, reconstruction) and global alignment objectives that teach semantic consistency with language (contrastive VLA losses) [21]. Finally, many 2D VLA recipes succeed because they can exploit huge negative sets and large effective batch sizes. In 3D those levers are severely limited by memory and computation. The problem is further amplified in medical imaging, as radiology reports and diagnostic codes often list multiple co-occurring conditions. Hence, candidate “negatives” frequently share clinical semantics with positives. This overlap weakens the signal from standard CLIP-style contrastive losses.

These technical constraints motivate a set of open ques-

tions about how to build scalable, generalizable 3D foundation models. In this work, we treat these questions as the central technical problems rather than as secondary engineering constraints. Specifically, we introduce SPECTRE, a transformer-based 3D CT foundation model trained on industrial-grade hardware. Our framework emphasizes (1) geometry-aware transformer design and tokenization to encode anisotropy and voxel-scale information explicitly, (2) attention architectures and computational strategies that balance token complexity and context preservation for large-scale volumetric data, and (3) a two-stage pretraining pipeline that combines SSL and VLA objectives; using SSL-like objectives to bootstrap robust geometry-aware features, followed by VLA to inject clinical semantics. We empirically analyze how these design choices affect downstream transfer across tasks that span region-level localization, classification, and study-level semantic retrieval. To support future research on scalable medical foundation models, we publicly release SPECTRE, along with all training code and pretraining recipes, as a fully open-source foundation for the community. An overview of the SPECTRE architecture and pretraining is presented in Fig. 2.

## 2. Related Works

### 2.1. 3D Vision Transformers

Recent transformer-based architectures have been extended to 3D medical volumes to capture global context beyond the reach of local convolutions. Early models embed a transformer encoder within a U-shaped network: for example, UNETR [23] uses a pure transformer backbone to encode the entire volume as a sequence, then connects multi-scale features via U-Net skip-connections. Similarly, nnFormer [64] interleaves convolutional stems with transformer blocks and adds novel volume-based self-attention and “skip attention” for U-Net connections. These hybrid designs exploit convolutions for local detail while leveraging self-attention for long-range dependencies.

Hierarchical and windowed attention schemes have also been popular. Swin-style 3D transformers embed patches hierarchically: SwinUNETR [22] uses 3D windowed attention to build a multi-resolution encoder-decoder. The original SwinUNETR achieved SOTA on several benchmarks, and SwinUNETR-V2 [25] further inserts convolutional layers before each Swin block to reintroduce spatial bias, yielding a stronger backbone that generalizes across tasks with a single recipe. These models downsample tokens to form feature pyramids, enabling efficient computation on large volumes.

More recent pure-transformer architectures eliminate convolutions entirely and refine the fundamental ViT components for volumetric data. Primus [55] introduces the first fully transformer 3D segmentation network, preserv-

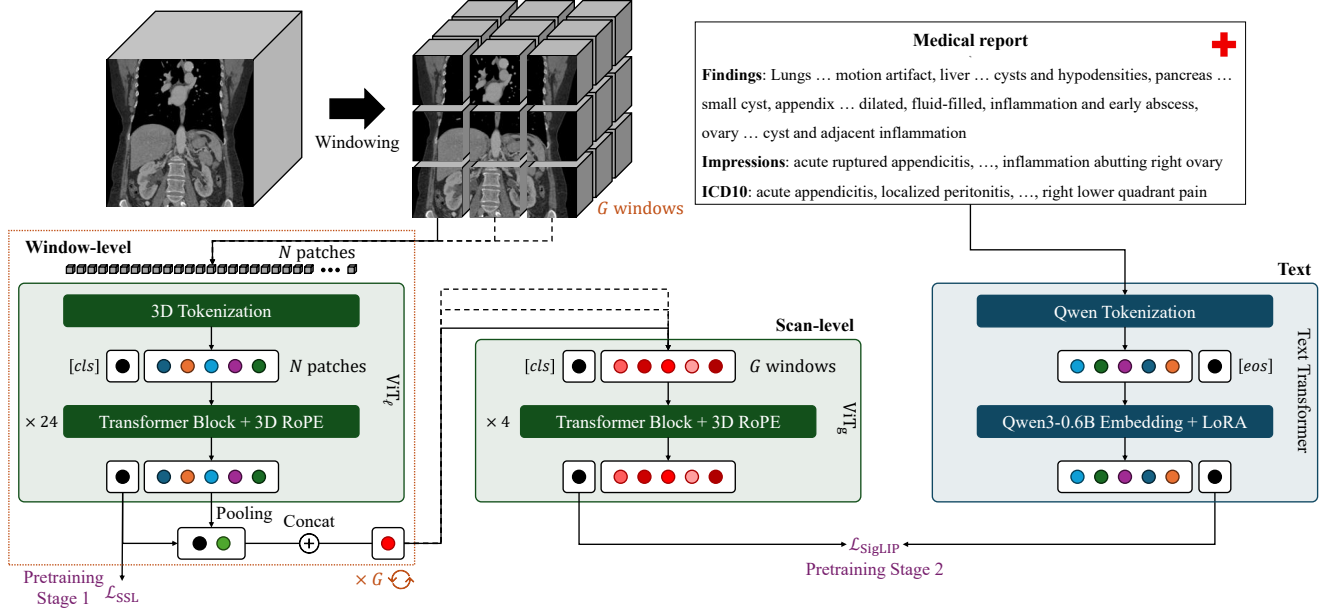


Figure 2. Overview of the proposed multimodal CT-report model. The model jointly processes volumetric CT data and corresponding radiology reports. The local vision transformer  $\text{ViT}_\ell$ , pretrained using DINOv3 (Stage 1), extracts localized image features from CT volume crops. These features are aggregated by the global vision transformer  $\text{ViT}_g$ , while the text transformer encodes the associated medical report. During SigLIP pretraining (Stage 2), the vision and text representations are aligned in a shared embedding space.

ing high-resolution tokens and employing improved block designs with 3D rotary positional embeddings (RoPE) to encode volumetric geometry. SuperFormer [18] generalizes Swin Transformer [38] to 3D super-resolution via volumetric patch embeddings, 3D relative positional encoding, and shifted window attention, whereas WaveFormer [2] integrates multi-scale wavelet transforms inside the transformer to retain high-frequency detail with reduced complexity. Across these models, volumetric patch embeddings replace 2D patches with 3D cubes, while attention is commonly employed within local 3D windows or solely in the axial direction.

SPECTRE builds on these advances with a fully volumetric transformer backbone tailored to CT. It adopts anisotropic 3D patch embeddings aligned with CT voxel geometry and employs 3D RoPE for volumetric relative positioning, but extends it with DINOv3-style stochastic shifts [52] during pretraining to increase robustness to variable voxel spacing and FOV. Further, SPECTRE uses a two-stage attention design combining dense local attention with coarse global attention, and is trained at foundation scale on a large unlabeled CT corpus, enabling general-purpose volumetric representation learning.

## 2.2. CT Foundation Models

In CT imaging, *foundation models* leverage large unlabeled datasets or rich supervision. CT-CLIP [21] and Merlin [7] align 3D CT with text. CT-CLIP uses  $\approx 25,000$  chest CTs

and a CLIP-style loss [48] for joint embeddings, excelling at retrieval and detection. Merlin trains on  $\approx 15,000$  abdominal CTs with reports and EHR labels, enabling strong zero-shot classification, retrieval, report generation, and segmentation. These VLA models are effective but region-specific. MedImageInsight [13] takes a slightly different approach and scales to diverse modalities, including X-ray, CT, and MRI. However, it may under-emphasize fine CT anatomy compared to CT specific models.

A second family uses SSL on large unlabeled CT datasets. CT-FM [46] pre-trains on 148,000 mixed volumes with contrastive objectives, achieving state-of-the-art segmentation, triage, retrieval, and semantic performance on several tasks while clustering anatomical regions. FM-CIB [45] contrastively pre-trains on 11,467 lesion patches for biomarker prediction, outperforming “from scratch” and ImageNet [14] baselines and correlating with tumor biology. VoCo [59] adds region-level context prediction by identifying anatomical location from “base” crops. SSL models capture strong image features, however, they may lack explicit clinical semantics.

Some models target segmentation. VISTA3D [26] unifies supervised and interactive segmentation through a CNN encoder and promptable interface. SuPreM [37], built on aggregated labeled datasets [36], pre-trains supervised 3D encoders with high transfer performance. These models show excellent performance on segmentation tasks, but depend on dense labels and focus narrowly on anatomy.

PASTA [35] takes a generative approach and uses 30,000 synthetic CTs with tumor annotations and reports to pre-train a model excelling on 45/46 downstream oncology tasks. Additionally, it builds a clinical decision-support system, improving radiologist accuracy. Synthetic pipelines reduce data scarcity but risk simulation bias and task specialization.

Earlier work like ModelsGenesis [66] showed that simple 3D SSL (*i.e.*, inpainting, shuffling) outperforms training from scratch and 2D ImageNet transfer, but remains small-scale and unimodal.

In summary, CT foundation models vary in modality (image-only vs. multimodal), body coverage, and pretraining strategy. Most VLA models target one region and one modality, while vision-only SSL models focus on image features without language. Segmentation models emphasize per-voxel labels. SPECTRE integrates these strengths: multi-region CT pretraining, a pure 3D ViT with explicit geometry encoding, and a two-stage pipeline that first learns robust SSL-like primitives and then adds clinical semantics via VLA on report-paired data, combining fine 3D detail with broad clinical understanding in an open-source, scalable framework.

### 3. Efficient 3D Transformer-Based Modeling

We aim to keep the model architecture as close to the plain ViT architecture [15] as possible while introducing only the minimal, principled adaptations required for volumetric CT. Our resulting model, SPECTRE, follows a two-stage transformer design consisting of a local ViT ( $\text{ViT}_\ell$ ) and global ViT ( $\text{ViT}_g$ ) components.  $\text{ViT}_\ell$  encodes fine-grained, geometry-aware representations from local 3D regions, while  $\text{ViT}_g$  aggregates these region-level tokens to capture scan-level semantics and long-range dependencies. This hierarchical structure (1) preserves the simplicity and transferability of the ViT backbone, (2) enables explicit, low-cost pathways for both localized reasoning and global context modeling, and (3) retains full compatibility with existing adapter and decoding architectures. SPECTRE benefits from an ad-hoc 3D tokenization process along with custom positional encodings and attention mechanism that tailor the ViTs to the specific requirements of CT imaging.

#### 3.1. Minimal 3D Tokenization

Given a CT volume  $X \in \mathbb{R}^{H \times W \times D}$ , the first stage partitions  $X$  into non-overlapping 3D patches  $P_i(X)$  and applies a linear projection to obtain token embeddings  $T^{(0)}$ :

$$T^{(0)} = [x_1, \dots, x_N]^\top, \quad x_i = E(P_i(X)) \in \mathbb{R}^d, \quad (1)$$

where  $E(\cdot)$  is a linear mapping of the flattened patch. In all experiments, patches are chosen with spatial size  $H_p \times W_p \times D_p = 16 \times 16 \times 8$  voxels. The patch depth  $D_p$

is set to half the in-plane patch size, as voxel spacings in the slice direction are typically about twice as large as those in the axial plane. The embedding dimension is set to  $d = 1080$ , providing a balance between efficiency and resolution. This design corresponds to an effective compression factor of  $\frac{2048}{1080} \approx 1.8962$ .

For a typical volume crop of  $H, W = 128, D = 64$  voxels, representative for many downstream applications (*e.g.*, lesion segmentation), the above yields 512 tokens, equal to the number of patches obtained from a 2D image of size  $256 \times 256$  using a patch size of  $16 \times 16$ .

#### 3.2. Local and Scan-Level Attention

$\text{ViT}_\ell$  implements standard Transformer layers but with attention restricted to local windows. We partition the token grid of a full CT scan into  $G$  windows (corresponds to 3D crop of the CT volume), each consisting of  $m$  tokens. Each local window is prepended with a learnable [cls] token  $c_w \in \mathbb{R}^d$  whose final state encodes a compact summary of window-level context. For a window token matrix  $T_w \in \mathbb{R}^{(1+m) \times d}$ , we compute Multi-Head Self-Attention (MHSA) as usual:

$$\text{Attn}(T_w) = \text{softmax}\left(\frac{QK^\top}{\sqrt{d_k}}\right)V, \quad (2)$$

$$Q = T_w W_Q, \quad K = T_w W_K, \quad V = T_w W_V. \quad (3)$$

The per-layer cost across the whole scan is

$$\text{Cost}_{\text{global}} = G \cdot \mathcal{O}(m^2 d), \quad (4)$$

which is linear in  $G$  for fixed  $m$ . After processing by  $\text{ViT}_\ell$ , each window  $w$  produces a set of patch tokens  $T_{w,i=2}^{(\ell)}$  together with a window-level [cls] token  $T_{w,1}^{(\ell)} = c_w$ . We obtain a compact representation suitable for scan-level aggregation as

$$\bar{t}_w = \frac{1}{m-1} \sum_{i=2}^m T_{w,i}^{(\ell)} \in \mathbb{R}^d. \quad (5)$$

Then we concatenate  $\bar{t}_w$  with the [cls] token to form a single representation for each window:

$$u_w = [c_w \parallel \bar{t}_w] \in \mathbb{R}^{2d}, \quad w = 1, \dots, G. \quad (6)$$

This design preserves global contextual information from  $c_w$  and reduces the token count by summarizing patch-level detail into a single descriptor, thereby controlling memory usage in subsequent stages. The per-window vectors are stacked into a matrix

$$U = [u_1, \dots, u_G]^\top \in \mathbb{R}^{G \times 2d}. \quad (7)$$

Before entering the global encoder, the sequence is linearly projected back to dimension  $d$  to obtain  $\tilde{U}$ . A learnable

scan-level [cls] token  $c_g \in \mathbb{R}^d$  is prepended to  $\tilde{U}$  to form the input to the global encoder:

$$Z = \begin{bmatrix} c_g \\ \tilde{U} \end{bmatrix} \in \mathbb{R}^{(G+1) \times d}. \quad (8)$$

The global encoder  $\text{ViT}_g$  computes full MHSA over  $\mathcal{T}_g$ :

$$T^{(g)} = \text{ViT}_g(Z) \in \mathbb{R}^{(G+1) \times d}. \quad (9)$$

Because  $G \ll m$ , attention in  $\text{ViT}_g$  remains computationally efficient while aggregating scan-level semantics.

### 3.3. 3D Rotary Positional Encoding

The proposed architecture employs 3D rotary positional embeddings (RoPE) [53]. RoPE injects continuous axial coordinates by rotating query and key vectors rather than by adding learned vectors, which avoids storing large interpolated fields while preserving relative-position information across resolutions. Each attention head has dimension  $d_k$  (so  $d_k = d/H_s$  or  $d_k = d/H_g$  depending on encoder), and by setting

$$d_k \equiv 0 \pmod{6}, \quad (10)$$

SPECTRE allocates  $L = d_k/6$  frequency slots per axis.

To further improve robustness to resolution and scale changes, RoPE-box jittering is implemented as in DINOv3 [52], applying only a global rescaling with  $s \sim \mathcal{U}(0.5, 2.0)$  to the normalized coordinates  $r_i \in [-1, 1]^3$  obtaining  $\tilde{r}_i$ . With shared frequency periods  $p \in \mathbb{R}^L$ , axis angles are

$$\theta_i^{(a)} = 2\pi, \tilde{r}_i^{(a)}/p, \quad (a \in h, w, d), \quad (11)$$

and we define

$$\cos_i = \cos(\Theta_i), \quad \sin_i = \sin(\Theta_i), \quad (12)$$

where  $\Theta_i$  is the concatenated per-axis angle vector.

RoPE is then applied to query and key projection heads via the rotate/merge matrix  $\mathcal{R}$ :

$$Q' = \mathcal{R}(Q; \cos_i, \sin_i), \quad K' = \mathcal{R}(K; \cos_i, \sin_i). \quad (13)$$

Using RoPE in both  $\text{ViT}_\ell$  and  $\text{ViT}_g$  ensures robustness to local window size, resolution, and varying numbers of windows per scan.

## 4. DINO-Driven Vision-Language Pretraining

We divide pretraining into two complementary stages. The first stage optimizes a self-supervised learning (SSL) objective that encourages the model to capture fine-grained local visual features from CT volumes. The second stage aligns image-text pairs under weak supervision, extracting semantically meaningful cues from medical reports as well

as global scan-level features. Together, these stages enable both detailed spatial understanding and semantic alignment with clinical knowledge. Details about the data pipelines, data preprocessing, hyperparameters, and pretraining hardware can be found in the *Supplementary Material*.

### 4.1. Self-Supervised Local Representation Learning

The first pretraining stage employs an adapted version of the DINOv3 framework [52]. The framework leverages a student-teacher pair of ViTs built on the  $\text{ViT}_\ell$  backbone, both of which produce a [cls] token of embedding size  $d = 1080$ . A three-layer projection head is attached to the backbone to produce the high-dimensional prototypes used for distillation. The student is a masked ViT [24] where a subset of input patch tokens is replaced by a learnable mask token before encoding. The teacher is an exponential moving average of the student and provides stable soft targets for distillation.

Input views are created by a multi-crop strategy by sampling two global views and eight local views from each input CT volume. Global views are sampled with independent scale ratios on each axis drawn as  $r_g \sim \mathcal{U}(0.5, 1.0)$  and rescaled to 0.5 of the original volume. Local crops are sampled with ratios  $r_\ell \sim \mathcal{U}(0.1875, 0.5)$  and rescaled to 0.1875 of the original volume. In addition to random resized cropping, augmentations applied to all views include: (1) random flipping along each anatomical axis with probability  $p = 0.5$ , (2) Gaussian sharpening or Gaussian smoothing with  $p = 0.25$  (mutually exclusive), (3) gamma intensity transforms with  $p = 0.25$ , (4) additive Gaussian noise with  $p = 0.25$ , and (5) random intensity rescaling with  $p = 0.5$ . The rescaling window is sampled by choosing

$$w_{low} \sim \mathcal{U}(-1000, -200), \quad w_{high} \sim \mathcal{U}(+200, +1000), \quad (14)$$

and voxel intensities are linearly rescaled to unity range within that window.

Similar to the DINOv2 [44] and DINOv3 [52] implementations, we jointly optimize the DINO [9], iBOT [65] and KoLeo [49] training objectives with relative weights of  $1 : 1 : 0.1$ . In contrast to DINOv3, we deliberately omit the Gram loss term (primarily relevant in the optimization of dense features when scaling models to billions of parameters) due to the relatively narrow operational spectrum of the CT domain. The DINO term enforces global consistency between teacher and student across scales. With  $\mathcal{G}$  denoting the set of global crops and  $\mathcal{H}$  the set of local crops, the DINO loss is computed as the cross-entropy between the teacher’s global soft targets and the student’s predictions on

all other views:

$$\mathcal{L}_{\text{DINO}} = \frac{1}{D} \sum_{g \in \mathcal{G}} \sum_{\substack{v \in \mathcal{G} \cup \mathcal{H} \\ v \neq g}} \sum_{k=1}^K (-q_t^{(k)}(g) \log p_s^{(k)}(v)), \quad (15)$$

where  $q_t(g)$  is the teacher softmax on the DINO head for global crop  $g$ ,  $p_s(v)$  is the student softmax on crop  $v$ , and  $D = |\mathcal{G}|(|\mathcal{G}| + |\mathcal{H}| - 1)$  the number of combinations.

The iBOT term performs masked patch self-distillation. Let  $\mathcal{M}$  denote the set of masked patch positions and let  $C$  denote the token vocabulary size for the token-wise head. The iBOT loss is the average token-level cross-entropy over masked patches:

$$\mathcal{L}_{\text{iBOT}} = \frac{1}{|\mathcal{M}|} \sum_{m \in \mathcal{M}} \sum_{c=1}^C (-q_t^{(c)}(m) \log p_s^{(c)}(m)), \quad (16)$$

where  $q_t^{(c)}(m)$  are the teacher’s soft targets for token class  $c$  at patch  $m$  and  $p_s^{(c)}(m)$  are the student’s predicted token probabilities at the same position. In this setup, the teacher produces token-level targets from global views in which a fraction of tokens are replaced by a mask token, and the student is trained to predict these targets at the masked positions. We apply masking to 50% of the global views within each batch and randomly mask a proportion  $\rho \sim \mathcal{U}(0.2, 0.7)$  of tokens. This range is higher than the  $\mathcal{U}(0.1, 0.5)$  used in DINOv3 and the original iBOT implementation, reflecting the reduced difficulty of the task in 3D, where each token has a larger number of spatial neighbors. We use separate projection heads for the DINO and iBOT objectives and set the number of output prototypes  $K = C = 65,536$ .

Finally, KoLeo provides a regularization that encourages a uniform spread of the embeddings to prevent collapse and promote effective use of the representation space. For a batch of L2-normalized embeddings  $z_i$ , the loss identifies, for each embedding, its nearest neighbor  $z_i^{\text{NN}}$  based on cosine similarity and penalizes small distances:

$$\mathcal{L}_{\text{KoLeo}} = -\frac{1}{N} \sum_{i=1}^N \log (\|z_i - z_i^{\text{NN}}\|_p + \varepsilon), \quad (17)$$

where  $\|\cdot\|_p$  denotes the  $p$ -norm ( $p = 2$ ) and  $\varepsilon$  is a small constant for numerical stability. The nearest neighbor  $z_i^{\text{NN}}$  is the embedding in the batch with a maximal cosine similarity to  $z_i$  that excludes itself.

## 4.2. Global Clinical Context Alignment

Following self-supervised pretraining of  $\text{ViT}_\ell$ , the full model is aligned with free-text clinical reports using the SigLIP objective [61].

Each preprocessed scan is partitioned into  $G = 36$  windows of size  $128 \times 128 \times 64$  voxels, and encoded by the

full model ( $\text{ViT}_\ell$  and  $\text{ViT}_g$ ) into a feature vector of embedding size  $d = 1080$ . Radiology text is encoded with the Qwen3-0.6B Embedding model [63] augmented with low-rank adapters (LoRA; rank  $r = 16$ ,  $\alpha = 64$ ), while image and text embeddings are projected into a shared 512-dimensional space using three-layer projection heads. The embeddings are  $L_2$ -normalized before similarity computation. To allow efficient computation of all image–text pair similarities across a compute cluster, text embeddings are shuffled across devices while image embeddings remain local, allowing the use of a large set of negatives without excessive communication.

The SigLIP loss replaces the softmax-based InfoNCE [43] used in conventional methods such as CLIP [48] with binary cross-entropy terms based on symmetric sigmoids. The sigmoid-based terms better accommodate the inherently noisy and many-to-many nature of vision-text pairs in clinical datasets, where a single scan may correspond to multiple textual descriptions of varying granularity. Furthermore, losses based on sigmoid have shown to be less sensitive to small batch sizes compared to their softmax-based counterparts [61].

Let  $v_i$  and  $t_i$  denote the normalized image and text embeddings for the  $i$ -th paired sample, and let  $\tau > 0$  be a temperature. Define the scaled cosine similarity

$$\text{sim}(v, t) = \frac{\langle v, t \rangle}{\tau}. \quad (18)$$

The directional SigLIP loss from images to text is written as

$$\mathcal{L}_{v \rightarrow t} = -\frac{1}{N} \sum_{i=1}^N \left[ \log \sigma(\text{sim}(v_i, t_i)) + \frac{1}{N-1} \sum_{j \neq i} \log (1 - \sigma(\text{sim}(v_i, t_j))) \right]. \quad (19)$$

with  $\sigma(x) = (1 + e^{-x})^{-1}$ . The total SigLIP loss averages in both directions as

$$\mathcal{L}_{\text{SigLIP}} = \frac{1}{2} (\mathcal{L}_{v \rightarrow t} + \mathcal{L}_{t \rightarrow v}), \quad (20)$$

where  $\mathcal{L}_{t \rightarrow v}$  is defined analogously by swapping image and text embeddings. This symmetric formulation ensures reciprocal alignment, while retaining the robustness advantages of the sigmoid-based objective.

## 5. Experiments

### 5.1. Cancer Image Biomarker Prediction

To assess the discriminative power and generalizability of volumetric representations, we adopt the standardized evaluation protocol of Pai et al. [47] and apply it uniformly across all CT foundation models under comparison. For

each model, frozen encoder embeddings are extracted and used to train a k-nearest neighbor (kNN) classifier without finetuning, enabling a controlled comparison of representation quality independent of task-specific optimization.

We assess performance on six datasets spanning diagnostic and prognostic objectives: malignancy prediction on LUNA16 [50] and DLCS [57], and two-year survival prediction on NSCLC-Radiomics [1], NSCLC-Radiogenomics [4], C4KC-KiTS [27], and Colorectal-Liver-Metastases [51]. Each dataset provides patient-level tumor biomarkers derived from volumetric CT scan crops, allowing consistent evaluation across diverse clinical endpoints.

All models are trained and evaluated under identical protocols to ensure fair comparison with prior benchmarks. Quantitative results are summarized in Fig. 1. Additional implementation details, as well as further quantitative and qualitative analyses are provided in the *Supplementary Material*.

## 5.2. Semantic Segmentation

To assess whether the representations learned by our volumetric CT transformer transfer to dense prediction, we conduct a series of controlled semantic segmentation experiments on established abdominal and renal CT benchmarks. Our goal here is not to build the strongest task-specific segmentor – with heavy, decoder-centric engineering – but to isolate encoder quality under realistic 3D conditions. We therefore follow the Encoder-only Mask Transformer (EoMT) [34] approach and extend it to the volumetric case: the pretrained SPECTRE encoder produces a set of volumetric tokens, and we instantiate a fixed set of learnable query tokens, one per semantic class in the target dataset. This removes the need for instance-level matching (no Hungarian, no dynamic query allocation) and allows us to supervise the model with standard voxel-wise losses (CE/Dice) on class masks. Importantly, this approach does predict masks at  $\frac{1}{4}$  of the input resolution. Specifically, given an input of size  $H \times W \times D$ , the model predicts masks on a feature grid of size  $\frac{H}{4} \times \frac{W}{4} \times \frac{D}{4}$  to keep computation feasible, and the features are subsequently upsampled to  $H \times W \times D$  using simple trilinear interpolation for evaluation. Fig. 5 depicts our implementation for semantic segmentation. We integrate the model as a drop-in replacement in nnU-Net to ensure comparability with widely accepted 3D medical segmentation practice, keeping the rest of the pipeline predominantly the same so that any gain can be attributed to representation quality rather than to the data augmentation, optimization strategy or model decoder. We call this adaptation to semantic segmentation with the EoMT model, Semantic Encoder only Masked Transformer (SEoMT). An in-depth discussion on the implementation details can be found in the *Supplementary Material*.

Table 1. Segmentation test results over 4 datasets. Average Dice of all five folds of the test datasets. Kidney tumor segmentation on KiTS23 dataset uses 4 folds.

	Method	Dice (%) ↑			
		AMOS-CT	KiTS23	LiTS	WORD
Conv.	nnU-Net [29]	<b>88.87</b>	85.99	79.29	83.11
	nnU-Net ResEnc L [30]	-	<b>88.06</b>	<b>81.20</b>	<b>85.79</b>
Transformers	CoTr [60]	77.13	84.63	78.44	83.11
	nnFormer [64]	85.63	75.72	77.02	82.53
	SwinUNETRv2 [25]	86.37	75.07	73.27	78.99
	UNETR [23]	78.33	76.33	70.91	70.87
	WaveFormer [2]	-	80.61	-	-
	Primus-M [55]	-	86.13	79.52	83.19
	Primus-L [55]	-	86.04	79.90	82.99
SPECTRE (ours)		<b>87.55</b>	<b>86.64</b>	<b>80.14</b>	<b>83.31</b>

We benchmark on the CT-heavy suite recommended by Isensee et al. [30], AMOS22 Task 1 (AMOS-CT) [32] (multi-organ, 15 classes), KiTS23 [27] (kidney + tumor + cyst), LiTS [6] (liver + lesion), and an additional abdominal CT set WORD [40]. These datasets jointly probe large, high-SNR organs with stable shape priors, and small, low-contrast tumor targets that are disproportionately sensitive to attention placement. We tuned model parameters on Fold 0 of the KiTS23 dataset during development, and thus, exclude that fold from the final result. For all other experiments across all the data folds over each dataset we use *exactly* the same model hyperparameters to ensure fair comparison with prior work. The quantitative results of our experiments are reported in Tab. 1 and selected qualitative results are available in Fig. 6. The results for the other models on AMOS-CT are obtained from [32]. For further details on the evaluation refer to the *Supplementary Material*.

## 5.3. Zero-Shot Text-to-Image Retrieval

To evaluate the cross-modal alignment capabilities of our full-scan representations, we perform zero-shot text-to-image retrieval experiments on two large-scale radiology datasets: CT-RATE [21] and Merlin [7]. Our objective is to assess how well the learned embeddings capture clinically meaningful relationships between volumetric CT data and free-text radiology reports, without any task-specific finetuning.

Following standard practice, both image and text inputs are projected into a shared latent space, and retrieval is performed by computing cosine similarity between modality embeddings. For CT-RATE, we use the validation split and evaluate recall-based retrieval metrics at various thresholds (Recall@K). The Merlin benchmark further enables analysis of report section granularity, providing Findings-to-Image and Impressions-to-Image retrieval tasks on its provided test split. We additionally evaluate a combined setting where both sections are jointly encoded to form a unified

Table 2. Text-to-image retrieval performance on full radiology reports of the validation set of CT-RATE [21] (N=1,564), including both *Findings* and *Impressions* sections.

Method	Recall@K (%) ↑			
	K=5	K=10	K=50	K=100
CT-CLIP [21]	2.9	5.0	18.0	28.8
SPECTRE (ours)	<b>17.5</b>	<b>25.5</b>	<b>48.9</b>	<b>59.9</b>
Random chance	0.3	0.6	3.2	6.4

Table 3. Text-to-image retrieval performance on the test set of Merlin [7], separated for the different *Findings* and *Impressions* sections, and for the *Full Report* (=FR). Recall is calculated for different sizes of non-overlapping data pools N.

	Method	Recall@1 (%) ↑			Recall@8 (%) ↑		
		N=32	N=64	N=128	N=32	N=64	N=128
<i>Findings</i>	OpenCLIP [12]	3.3	1.7	0.9	25.0	12.5	6.1
	BioMedCLIP [62]	4.4	2.1	1.2	30.6	15.6	7.9
	Merlin [7]	<b>77.6</b>	<b>68.7</b>	<b>59.4</b>	<b>98.8</b>	<b>96.5</b>	<b>92.0</b>
	SPECTRE (ours)	<b>55.5</b>	<b>43.8</b>	<b>33.0</b>	<b>93.5</b>	<b>86.3</b>	<b>76.1</b>
<i>Impressions</i>	OpenCLIP [12]	3.2	1.7	0.8	25.2	12.6	6.4
	BioMedCLIP [62]	4.6	2.4	1.2	32.2	16.9	8.1
	Merlin [7]	<b>38.4</b>	<b>27.7</b>	<b>19.4</b>	<b>85.4</b>	<b>70.6</b>	<b>56.4</b>
	SPECTRE (ours)	<b>43.2</b>	<b>32.9</b>	<b>24.0</b>	<b>83.7</b>	<b>72.8</b>	<b>61.5</b>
<i>FR</i>	SPECTRE (ours)	66.4	55.7	44.8	96.4	91.6	84.3
	Random chance	3.1	1.6	0.8	25.0	12.5	6.3

query representation.

All experiments are conducted using the pretrained SPECTRE encoder, Qwen3-0.6B Embedding model with LoRA adapters, and SigLIP projection heads without additional adaptation. Baselines include CT-CLIP [21] and the Merlin foundation model [7], as well as OpenCLIP [12] and BioMedCLIP [62]. Quantitative results are summarized in Tab. 2 and Tab. 3, while UMAP visualizations of the joint embedding space of SPECTRE are provided in the *Supplementary Material*.

## 6. Discussion

This research scales the pretraining of CT transformers by combining three key elements: a large collection of CT scans paired with radiology reports, transformer architectures specifically optimized for volumetric CT data, and state-of-the-art pretraining methods adapted from recent SSL and VLA advances.

The resulting foundation model, SPECTRE, delivers consistent improvements across diverse tasks. On tumor biomarker classification, our model achieves the best overall performance among prior CT foundation models, outperforming competitors on 4/6 tasks. This demonstrates that large-scale paired pretraining yields representations

that capture both structural and clinically meaningful information, enabling better discrimination of subtle biomarker-related patterns. For segmentation, our encoder-only framework surpasses all other domain-specific transformer-based models and performs competitively with nnU-Net, despite lacking any decoder-heavy design. Because the segmentation head simply interpolates the embedding vectors, the resulting predictions are remarkably smooth and anatomically coherent. However, this design can miss high resolution details when necessary - an area for improvement.

Beyond these supervised evaluations, SPECTRE exhibits strong cross-modal alignment. In full-scan text-to-image retrieval, it substantially outperforms CT-RATE, indicating robust visual-textual grounding. When analyzing retrieval from specific report sections, MERLIN performs best on the structured Findings text but struggles with the more interpretive Impressions section. In contrast, our model achieves the best results on Impressions-to-image retrieval and improves further when combining sections (Findings + Impressions), suggesting stronger integration across textual domains and less sensitivity to report structure. We attribute this to the language rewrites and text augmentations used during SigLIP-style pretraining, which enhance robustness to stylistic and structural variability.

Despite these advances, several limitations remain. Our pretraining corpus, though large, was skewed toward thoracic imaging, which may partly explain the stronger performance on lung-related tasks compared to abdominal ones. The reliance on clinical reports introduces inherent noise and bias, as descriptions vary in completeness and terminology across institutions. Furthermore, while the encoder-only segmentation approach offers elegance and computational efficiency, its smooth outputs can sometimes obscure small or faint lesions. Finally, even though training a large-scale foundation model requires substantial computational resources, sharing the trained model publicly enables broad reuse and mitigates the need for repeated training efforts. By releasing SPECTRE as an open, general-purpose 3D CT foundation model, we lower the barrier for institutions worldwide, enabling more accurate, data-efficient, and locally adapted medical imaging tools that can improve global health equity.

## 7. Conclusion

We presented SPECTRE, a fully transformer-based foundation model for volumetric CT and radiological reports understanding. The geometry-consistent, two-stage 3D Vision Transformer trained with large-scale self-supervision and subsequent report-level vision-language alignment with our text encoder, constitutes a single, task-agnostic volumetric backbone that performs well across heterogeneous medical imaging objectives. Without any decoder-heavy redesign, the pretrained 3D encoder both maintains SOTA-

level frozen transfer on 4/6 CT biomarker benchmarks and, in its encoder-only SEoMT form, reaches competitive performance on dense semantic segmentation tasks. At the same time, it preserves spatial discriminability under vision–language alignment, delivering strong CT–report retrieval and understanding. This establishes a scalable path toward general-purpose 3D medical foundation models.

## Acknowledgements

We express our sincere gratitude to the TU/e Supercomputing Center for providing access to the SPIKE-1 compute cluster and for their invaluable operational support. We further acknowledge SURF ([www.surf.nl](http://www.surf.nl)) for their assistance in enabling the use of the national supercomputer Snellius.

# Scaling Self-Supervised and Cross-Modal Pretraining for Volumetric CT Transformers

## Supplementary Material

Table 4. Overview of the datasets used for pretraining, summarizing anatomical coverage, the number of CT reconstructions remaining after all exclusions, and whether each dataset is used for self-supervised learning (SSL), vision–language alignment (VLA), or both.

Source dataset	Location	No. Rec.	SSL	VLA
NLST [54]	Chest	132,985	✓	
CT-RATE [21]	Chest	47,149	✓	✓
INSPECT [28]	Chest	23,226	✓	✓
Merlin [7]	Abdomen	15,314	✓	✓
AbdomenAtlas [36]	Abdomen	5,195	✓	
AMOS [32]	Abdomen	2,450	✓	
PANORAMA [3]	Abdomen	2,238	✓	
AbdomenCT-1K [41]	Abdomen	1,062	✓	
<b>Total</b>		<b>229,619</b>		

## A. Pretraining Data and Preprocessing

### A.1. Datasets

We curated a diverse collection of 3D CT scans from multiple publicly available datasets. Three of these datasets also include accompanying clinical metadata, such as radiology reports and EHR diagnostic codes, and can therefore be used for both SSL and VLA. Imaging data span the thoracic, abdominal, and pelvic regions and comprise a wide range of acquisition settings, including variations in radiation dose and the use of contrast agents. After applying exclusion criteria that are provided below for every dataset, the final set for pretraining comprises 229,619 image series. A summary of the datasets and their characteristics is provided in Tab. 4.

We now provide dataset-level summaries, including the filtering criteria and preprocessing steps used to construct the final pretraining corpus.

- **NLST** (the National Lung Screening Trial) [54] provides lung cancer screening data collected in the United States between 2002 and 2004. The dataset consists of low-dose helical chest CT scans from 26,254 participants with a two-year follow-up, yielding 73,116 studies. Owing to multiple reconstruction settings, the original release contains 203,099 series. For our purposes, we retain only one series per reconstruction kernel; if multiple series are available for the same kernel, we select the one with the largest number of slices. This yields at most two series per CT study, for a total of 132,985 image series. All

relevant DICOM series are converted into 3D volumes in NiFTi format.

- **CT-RATE** [21] provides paired 3D chest CT volumes and the corresponding radiology reports of 21,304 patients. It comprises 25,692 non-contrast chest CT studies, expanded to 50,188 series through multiple reconstructions. Each study is accompanied by the radiology report, including both *Findings* and *Impressions* sections, as well as multi-abnormality labels and metadata. The cohort is split into 20,000 patients for training and 1,304 patients for validation. To ensure data consistency, we excluded unintended head CT series by generating segmentation masks with the TotalSegmentator model [58] and removing scans where the proportion of voxels labeled as *brain* or *skull* was an outlier, with outliers defined by Tukey’s rule ( $Q3 + 1.5 \times IQR$ ) of the distribution of relative brain/skull volume. We also respect the original split and use only the original training set for pretraining of our model, resulting in a total of 47,149 image series for training.
- **INSPECT** [28] consists of CT pulmonary angiography (CTPA) scans paired with radiology reports that include the *Impressions* section. It contains imaging data from 19,402 patients with a total of 23,248 studies. To address data issues, we excluded partially uploaded files, resulting in a final set of 23,226 CTPA studies.
- **Merlin** [7] contains abdominal CT scans acquired at the Stanford Hospital Emergency Department between 2012 and 2018. It includes 25,494 studies from 18,317 patients, each paired with a radiology report comprising sections *Findings* and *Impressions*, as well as associated EHR diagnostic codes. The data is split into training, validation, and test sets, with 15,314 studies in the training set. We use the training split of the dataset in its provided form without applying further filtering or modifications to train our model.
- **AbdomenAtlas1.0Mini** [36] is a fully annotated publicly accessible subset of the larger AbdomenAtlas dataset, comprising 5,195 abdominal CT volumes with segmentations at the voxel-level. The annotations cover nine key anatomical structures: spleen, liver, left kidney, right kidney, stomach, gallbladder, pancreas, aorta, and inferior vena cava. The source images are aggregated from multiple existing public datasets, each of which contributes cases with varying imaging protocols, disease states, and anatomical coverage. For pretraining, we use only the raw CT scans without the accompanying segmentation labels.

- **AMOS** [32] is a multi-center dataset designed for multi-organ abdominal segmentation across diverse clinical scenarios. It comprises 500 CT and 100 magnetic resonance images (MRI) with voxel-level annotations for 15 abdominal organs, collected from multi-vendor and multi-phase acquisitions spanning a wide range of disease conditions. In addition, AMOS provides 1,900 unlabeled CT and 1,200 unlabeled MRI scans to support semi-supervised and unsupervised learning tasks. After excluding 50 corrupted or incomplete CT files, we retain a total of 2,450 CT scans for pretraining.
- **PANORAMA** [3] is a contrast-enhanced abdominal CT dataset designed to benchmark diagnostic performance for pancreatic ductal adenocarcinoma (PDAC) detection and diagnosis. It includes 2,238 anonymized CT scans acquired at two Dutch medical centers (Radboud University Medical Center and University Medical Center Groningen). The dataset was curated to ensure high-quality imaging and standardized acquisition protocols.
- **AbdomenCT-1K** [41] is a large and diverse abdominal CT dataset comprising 1,062 scans collected by aggregating multiple public single-organ datasets. It includes both contrast-enhanced and non-contrast studies with voxel-level annotations for four major abdominal organs: liver, kidneys, spleen, and pancreas. For our purposes, we use only the raw CT scans for pretraining.

## A.2. Image Processing for Self-Supervised Learning

For SSL with the adapted DINOv3, all CT series listed in Tab. 4 are first reoriented to a common anatomical coordinate system (right-left, anterior-posterior, superior-inferior; RAS) to ensure spatial consistency. The voxel intensities in Hounsfield Units (HU) are clipped to the range  $[-1000, +1000]$  to remove outliers and normalized to the unit range with 32-bit precision. Each scan is then resampled to a voxel spacing of  $0.5 \times 0.5 \times 1.0$  mm using trilinear interpolation and center-cropped to a maximum size of  $512 \times 512 \times 384$  voxels, sufficient to cover the FOV of most chest and abdominal scans while minimizing surrounding background. The resulting volumes are converted to 16-bit tensors and stored on disk. During training, these tensors are loaded into memory and a random crop of  $256 \times 256 \times 128$  voxels is extracted for each batch element. To further improve I/O efficiency, four random crops are sampled from the same CT scan and treated as separate batch elements.

## A.3. Data Processing for Vision-Language Alignment

For VLA with SigLIP, we first select the CT series that contain accompanying text from radiology reports or diagnostic codes (see Tab. 4). Following, all series are re-oriented to the RAS coordinate system, clipped within the

range  $[-1000, +1000]$  HU and normalized to a unity range, followed by resampling to a voxel spacing of  $0.75 \times 0.75 \times 1.5$  mm using trilinear interpolation. Again, we write the resulting tensors in 16-bit precision to disk and load accordingly during training.

To enhance textual descriptions, each paragraph in the radiology reports is expanded to multiple paraphrases. First, the reports are divided into two sections, *Findings* and *Impressions*, whenever these sections are provided. For each section, we prompt a large language model (LLM) to “rephrase clearly and concisely *without changing any medical facts*,” and to “*only* return the revised text”, ensuring clarity and consistency.

This prompt is supported by four examples curated by radiologists (two chest CT, two abdominal CT), demonstrating accurate rewrites that preserve clinical elements such as laterality, measurements, and negations. Using Google’s *Gemini 2 Flash*, we generate two additional paraphrases per section, resulting in three semantically equivalent versions. During training, a version is randomly sampled, following the LaCLIP single positive strategy [17], to provide clinically accurate supervision of vision-language alignment.

In addition to text, some reports include structured EHR diagnosis codes. Since LLMs struggle with raw codes (*e.g.*, J18.9), we replace each with its World Health Organization 2025 short description<sup>2</sup>. These are appended as a comma separated list at the end of the report to form a complete text input. The EHR descriptions are not rewritten and are added after LLM rewriting to preserve billing and epidemiological accuracy.

## B. Pretraining & Architectural Details

### B.1. Training and Model Configuration

Tab. 5 summarizes the training parameters for both SSL with DINOv3 and VLA with SigLIP. During VLA, the pre-trained  $\text{ViT}_\ell$  remains frozen for the first 10 epochs. To improve efficiency, all models are trained with mixed precision (FP16) and optimized using distributed data parallelism. Data loading is performed via GPU Direct Storage, enabling high-throughput I/O directly to device memory and thereby minimizing bottlenecks in large-scale training. Tab. 6 shows the architectural choices of SPECTRE, separated for the local  $\text{ViT}_\ell$  and global  $\text{ViT}_g$ . Note that during VLA, the LayerScale layers of  $\text{ViT}_\ell$  are initialized with the weights found during SSL.

### B.2. Hardware

Both pretraining phases of the foundation model are conducted on a cluster of three DGX B200 sys-

<sup>2</sup><https://www.who.int/standards/classifications/classification-of-diseases>

Table 5. Training hyperparameters during self-supervised learning (SSL) and vision–language alignment (VLA) pretraining stages; LR, LLRD, and WD denote learning rate, linear learning rate decay, and weight decay.

Hyperparameter	SSL	VLA
Epochs	150	100
Steps	83,100	59,000
Batch size	1,536	144
LR begin	$4 \times 10^{-3}$	$1 \times 10^{-4}$
LR end	$1 \times 10^{-6}$	$1 \times 10^{-6}$
LR schedule	Cosine annealing	Cosine annealing
LR warmup epochs	10	10
LLRD	0.9	0.9
WD begin	0.04	0.01
WD end	0.4	0.01
WD schedule	Inverse cosine annealing	Constant
Optimizer	AdamW ( $\beta_1 = 0.9, \beta_2 = 0.999$ )	AdamW ( $\beta_1 = 0.9, \beta_2 = 0.95$ )

Table 6. Architectural and model-scale specifications of the local ( $ViT_\ell$ ) and global ( $ViT_g$ ) parts of SPECTRE.

Configuration	$ViT_\ell$	$ViT_g$
Trainable parameters	339M	58M
Patch size	$16 \times 16 \times 8$	-
Layers	24	4
Embedding dimension	1,080	1,080
Attention heads	12	12
Position embedding	3D RoPE	3D RoPE
LayerScale initialization	0.1	1.0

tems (NVIDIA Corp., CA, USA), totaling 24 Blackwell GPUs with 4.32 TB of combined GPU memory. Each system contains 8 B200 GPUs (1.44 TB per DGX), dual Intel Xeon Platinum 8570 processors (112 cores, 224 threads), and 2.16 TB of system memory, yielding a cumulative 6.48 TB across the cluster. The three DGX systems are interconnected via high-speed InfiniBand, enabling efficient distributed training and data exchange.

## C. Downstream Experiments

### C.1. Cancer Image Biomarker Prediction

This section complements the analyses on the *Cancer Image Biomarker Prediction* experiments and provides additional details on the benchmark tasks, datasets, and evaluation setup used in the downstream cancer imaging experiments.

#### C.1.1. Foundation Models

We compare a comprehensive set of eleven publicly available CT foundation models: FMCIB [45], CT-FM [46], CT-CLIP [21], PASTA [35], VISTA3D [26], VOCO [59],

SUPREM [37], Merlin [7], MedImageInsight [13], ModelsGenesis [66], and our proposed SPECTRE. These models collectively represent the current generation of volumetric CT foundation models, spanning both unimodal (image-only) and multimodal (image–text) pretraining paradigms. More about these models can be found in the *Related Works* of the main paper and in the models’ respective papers.

#### C.1.2. Evaluation Framework

All models are evaluated within the standardized *TumorImagingBench* reference framework introduced by Pai et al. [47]. This framework ensures that embeddings are extracted under consistent preprocessing conditions, reproducing the *intensity normalization*, *crop sizes*, and *voxel spacings* used during each model’s original pretraining. Such harmonized extraction allows for direct comparison of representation quality across models without task-specific retraining. For SPECTRE, we use a default input size of  $128 \times 128 \times 64$  voxels with a voxel spacing of  $0.5 \times 0.5 \times 1.0$  mm. Since SPECTRE is trained agnostic to input crop size and spacing, we double the field of view for the *NSCLC-Radiogenomics* [4] and *Colorectal-Liver-Metastases* [51] datasets to ensure that all lesions are fully contained within the input volume. All other datasets use the default configuration.

#### C.1.3. Tasks & Datasets

The TumorImagingBench spans six public datasets covering diagnostic and prognostic tasks in thoracic, renal, and hepatic oncology. The benchmark includes two task types: (1) lung nodule malignancy classification, and (2) prediction of two-year survival across multiple tumor sites. A brief overview of the datasets used in our experiments is provided below.

- **LUNA16** [50]. A dataset containing 888 CT scans and 1,186 annotated lung nodules. We follow the established subset of 677 nodules enriched for malignancy suspicion. Task: *malignancy classification*.
- **DLCS** (Duke Lung Cancer Screening) [57]. A clinical lung-nodule cohort with 2,487 nodules from 1,613 patients; we adopt the publicly released portion with 1,714 scans and pathology-confirmed malignancy labels. Task: *malignancy classification*.
- **NSCLC-Radiomics** [1]. CT scans from 421 patients with stage I–IIIB non-small cell lung cancer (NSCLC) treated with radiation therapy, including expert Gross Tumor Volume (GTV) segmentations. Task: *two-year survival prediction*.
- **NSCLC-Radiogenomics** [4]. Surgical NSCLC cohort with preoperative CT/PET imaging; we use 133 cases with curated GTV segmentations. Task: *two-year survival prediction*.
- **C4KC-KiTS** [27]. Renal tumour cohort from partial or radical nephrectomy patients; after filtering for complete

segmentations and follow-up, 134 cases remain. Task: *two-year survival prediction*.

- **Colorectal-Liver-Metastases** [51]. Preoperative CT scans from 194 patients undergoing resection of colorectal liver metastases, using the largest lesion per patient. Task: *two-year survival prediction*.

#### C.1.4. Analysis

Further quantitative analyses on these tasks are provided in Fig. 3, which reports per-model performance with 95% confidence intervals. Notably, for LUNA16, DLCS, and NSCLC-Radiomics, tasks on which our model outperforms all competing approaches, the confidence intervals are narrow, indicating stable performance and low variance across cross-validation folds. In contrast, for NSCLC-Radiogenomics and Colorectal-Liver-metastases, tasks where we do not achieve SOTA performance, all models exhibit large confidence intervals and generally low scores. This is likely due to the smaller dataset sizes, which can introduce quantization noise in the AUC calculation and reflect the inherent difficulty of these tasks.

Additional qualitative evidence is shown in Fig. 4, which visualizes model explanations using saliency maps on non-curated CT samples. Without any task-specific finetuning, the model already attends to pathologic regions associated with tumor presence, indicating that the learned representations encode clinically relevant spatial features. This behavior supports the effectiveness of our pretraining strategy and echoes findings from earlier foundation-model studies demonstrating that large-scale contrastive or multimodal pretraining facilitates robust zero-shot localization and biomarker-related signal emergence [47].

## C.2. Semantic Segmentation

This section details the full protocol used to evaluate SPECTRE on volumetric *Semantic Segmentation* and makes explicit the detailed experiments that led to the final SEoMT configuration reported in the main paper and the results across the benchmarks obtained.

### C.2.1. Adapting EoMT to 3D Semantic Segmentation

To isolate the segmentation capability of the vision encoder itself, and not any task-specific head, we extend the Encoder-only Mask Transformer (EoMT) paradigm to volumetric (3D) semantic segmentation. In line to the original 2D EoMT, we remove all task-specific decoders and operate entirely on the encoder token space, also in the 3D case. The model starts from our SPECTRE 3D encoder ( $\text{ViT}_\ell$ ), which produces a sequence of anisotropic 3D tokens (CT patches) using the same tokenizer and 3D RoPE as in pretraining.

### C.2.2. Query Design for Semantic Segmentation (3D)

After an initial set of encoder blocks, we append a fixed set of learnable query tokens to this sequence. Because

semantic segmentation does not require instance enumeration, we set the number of learnable query tokens equal to the number of semantic classes in the dataset (e.g., 3 for liver, kidney, tumor). The remaining 3D encoder blocks then run joint self-attention over both volume tokens and class queries. This allows the queries to attend to spatial tokens and, symmetrically, lets spatial tokens condition on the queries, so no extra transformer decoder is required. At the output, we obtain (1) per-class embeddings from the queries and (2) a dense 3D feature grid from the encoder tokens. We project the 1/4-resolution feature grid to per-voxel class logits and trilinearly upsample it back to the original CT resolution to compute Dice and Cross-Entropy losses. Because the number of classes in medical CT is small and fixed, every query is forced to explain a coherent anatomical or lesion region, which stabilizes training and removes the need for Hungarian matching or instance-slot allocation.

### C.2.3. Integration into nnU-Net

To position this as a fair encoder-only test, we integrate SPECTRE directly into nnU-Net as a drop-in encoder replacement. Apart from replacing the encoder, no architecture-specific components (multi-scale FPN-style features, convolutions for scale mixing, mask transformer decoders, etc.) are introduced. This ensures the comparison measures “representation quality of the encoder” – not engineering around it. We overwrite some of the suggested training plans with new SPECTRE plans. The images are resampled to  $0.75 \times 0.75 \times 1.5\text{mm}$  and intensities are rescaled to 0-1 using the 0.5% and 99.5% datasets intensity profiles. Additionally we employ the optimizers and learning rate schedulers as suggested in [34], with an AdamW optimizer with a learning rate of  $1 \times 10^{-5}$ , weight decay  $3 \times 10^{-5}$  and gradient clipping of 1.0. Models are trained for 150 epochs with 250 steps per epoch and a batch size of 2, following the nosLL [56] finetuning pipeline. An nnU-Net Github branch with SPECTRE integration will be made publicly available upon paper acceptance.

### C.2.4. Datasets

To avoid unstable conclusions caused by noisy, small, or historically under-annotated radiology datasets, we follow the recommended large-scale segmentation benchmarks by Isensee et al. [30]. Since our approach focuses purely on CT imaging, we drop the datasets that contain MRI and add an additional CT datasets. Specifically we consider:

Dataset	# Volumes	Classes	Description
AMOS22-CT	300	15	Multi-organ CT
KiTS23	489	3	Kidney / tumor / cyst
LiTS	131	2	Liver + tumor
WORD	120	16	16 abdominal organs

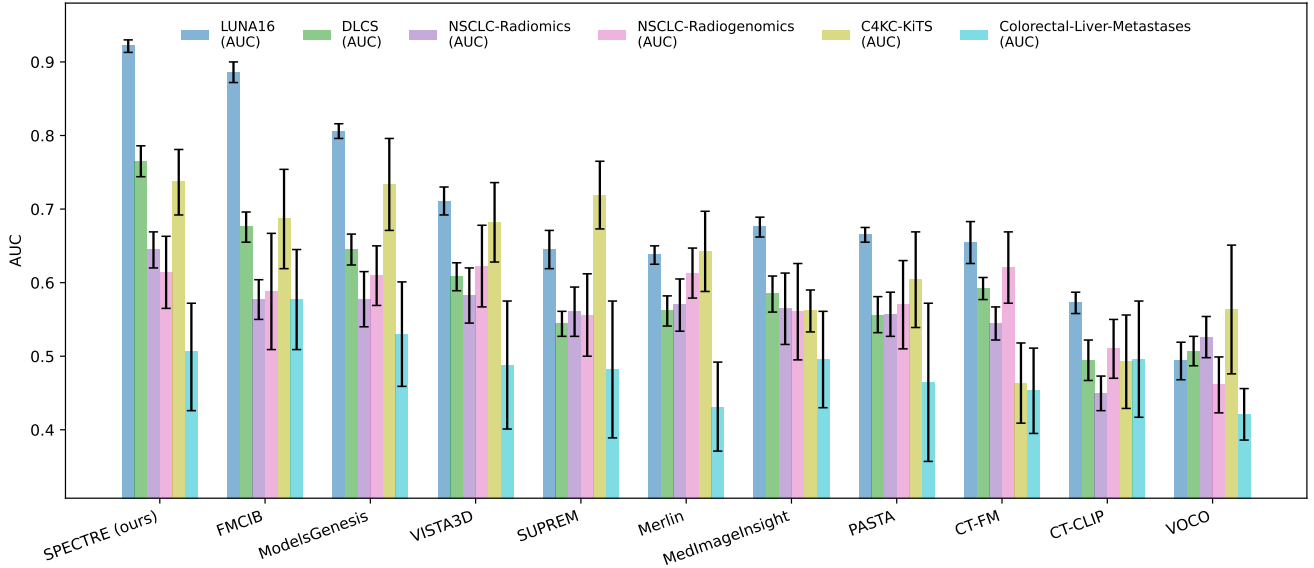


Figure 3. Quantitative comparison of 11 CT foundation models across six biomarker classification benchmarks using frozen-embedding kNN classifiers. Bars represent mean performance for each task, with error bars indicating 95% confidence intervals across cross-validation folds.

### C.2.5. Evaluation Protocol & Results

We adopt the evaluation protocol employed in Wald et al. [55]. All experiments are conducted within the nnU-Net framework [29], with the training set randomly divided into 80%/20% train/validation splits across 5 folds. After training, the model with the best pseudo Dice is used and validation on the validation set is automatically performed. We directly record the outcome of that result and thus the average of 5-fold cross-validation. For KiTS23, we tuned SPECTRE on *fold-0* during development and exclude that fold from the final reported cross-validation to avoid optimism. All other folds and datasets use exactly the same hyperparameters to make the cross-dataset comparison meaningful.

We compare SPECTRE against various 3D domain-specific segmentation architectures. Specifically, we consider nnU-Net [29] and the updated state-of-the-art ResNet-based nnU-Net ResEnc Large [30] for comparison with convolutional-based models. Recently many transformer-based models have been developed for segmentation in 3D data. We include CoTr [60], nnFormer [64], Swin-UNETRv2 [25], UNETR [23], WaveFormer [2] and the recent Primus [55] model for comparison. The results of these models on KiTS23 and LiTS and WORD are obtained from Wald et al. [55]. In their experiments, the models were tuned on fold-0 of KiTS23 and LiTS, and thus, the average of the other four folds are used as the baselines. The results for the models on AMOS-CT are obtained from Ji et al. [32]. All results are reported in average Dice across all classes.

During model development, we evaluated the impact of optimization strategies and input crop sizes on downstream segmentation performance after finetuning. The corresponding ablation results are reported in Tab. 7. Within the nnU-Net framework, Stochastic Gradient Descent (SGD) constitutes the default optimizer; however, our experiments show that AdamW [39] consistently outperforms SGD. Additionally, applying Deep Supervision, the default implementation in nnU-Net which computes weighed segmentation losses on intermediate lower resolution layers of the model, further improves training stability and final segmentation performance. We additionally observed that, at smaller crop sizes, models initialized with VLA (SigLIP) weights outperform counterparts initialized with just SSL (DINO). Increasing the crop size improves overall performance across initializations, while the performance gap between SSL- and VLA-initialized models narrows, rendering them comparable. Based on these observations, all subsequent experiments employ AdamW with a learning rate of  $1 \times 10^{-5}$ , Deep Supervision enabled, and an input crop size of  $320 \times 320 \times 128$ .

Fig. 6 shows qualitative masks for multiple datasets; they illustrate the same pattern as the numbers: large organs are clean and contiguous with the ground truth labels, while small tumors are present but slightly smoothed—consistent with predicting at 1/4 resolution and upsampling. We chose not to add an extra refinement head to keep the experiment honest.

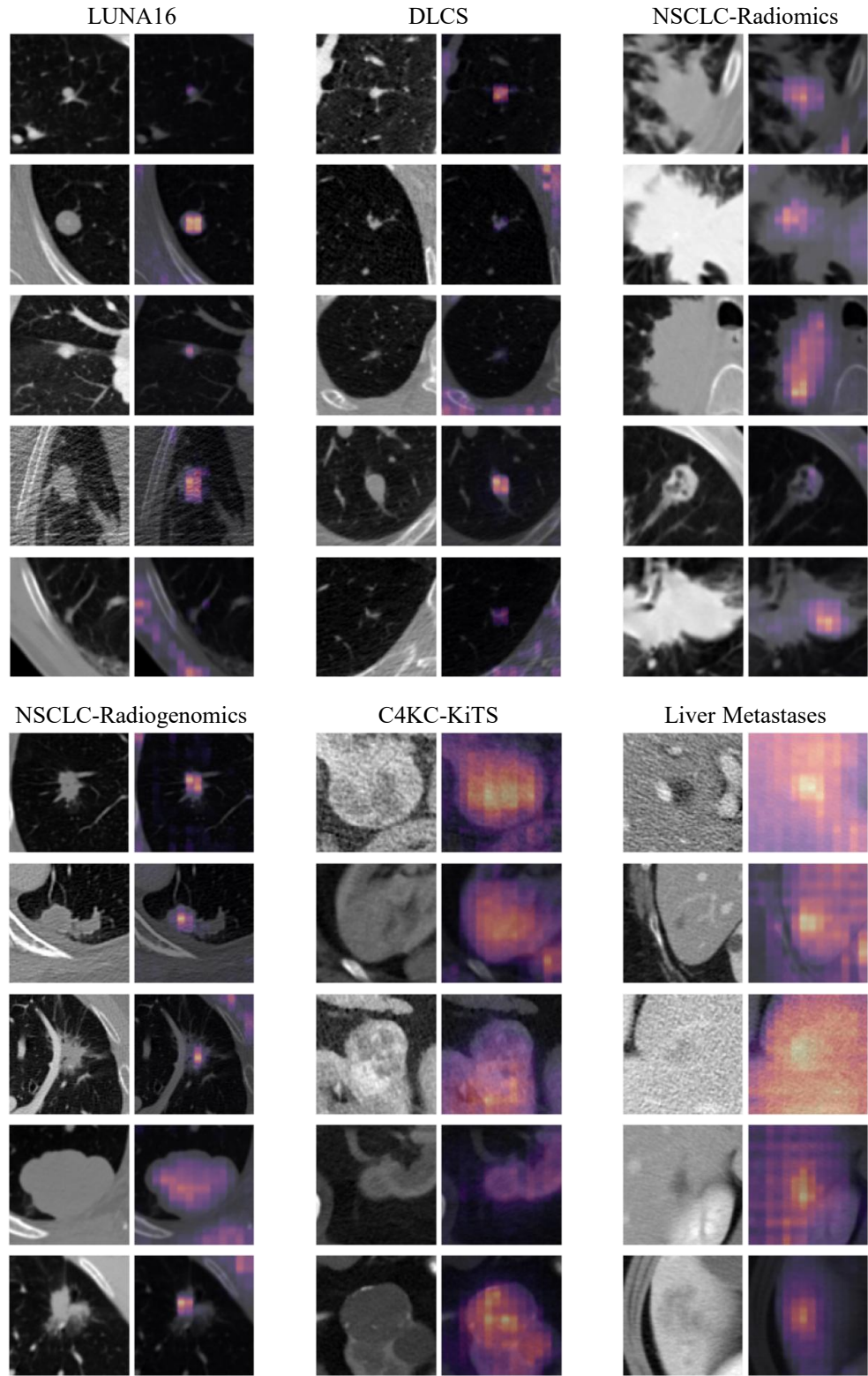


Figure 4. Non-curated saliency maps of SPECTRE on six tumor image biomarker datasets, obtained by occlusion sensitivity.

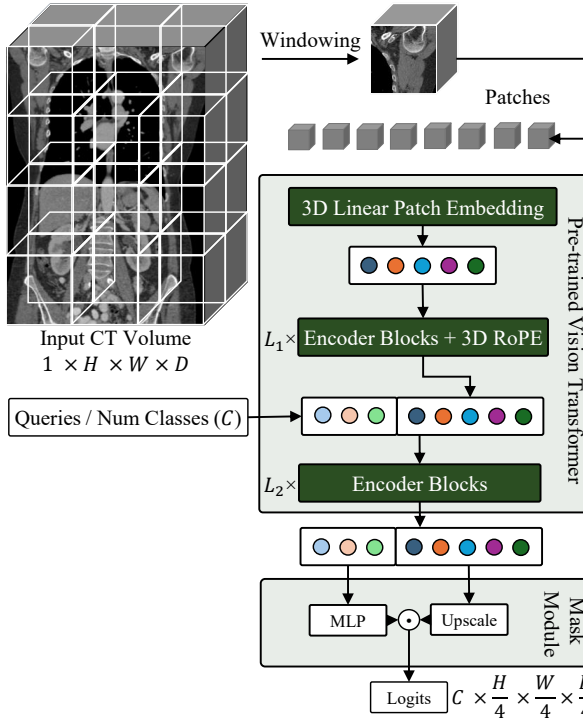


Figure 5. SEoMT architecture, derived from the EoMT. A learnable query for each class  $C$  is initialized and concatenated to the patch tokens. The new set of tokens are jointly processed by the last  $L_2$  blocks and used to predict logits corresponding to the semantic masks.

Table 7. Ablation experiments with the Kidney tumor segmentation on KiTS23 [27] dataset. Results in Dice on fold-0.

	SSL	VLA	Dice $\uparrow$
<i>Optimizer @ 320 x 320 x 128 input crop</i>			
SGD with LR $1 \times 10^{-4}$	✓	✓	DNF
SGD with LR $1 \times 10^{-5}$	✓	✓	0.763
AdamW with LR $1 \times 10^{-5}$ + Deep Supervision	✓	✓	0.868
<i>Crop Size</i>			
128 x 128 x 64	✓		0.854
128 x 128 x 64	✓	✓	0.862
320 x 320 x 128	✓		<b>0.871</b>
320 x 320 x 128	✓	✓	<b>0.871</b>

### C.3. Zero-Shot Text-to-Image Retrieval

For completeness, we report additional details on the zero-shot text-to-image retrieval experiments conducted in parallel to the downstream evaluations. Our goal is to align the protocol as closely as possible with prior work; all retrieval metrics and data splits follow the procedures described in

CT-RATE [21] and MERLIN [7].

For CT-RATE, we evaluate retrieval performance using both the *Impressions* and *Findings* sections of each radiology report. Following the original setup, each report is treated as a single textual query, and we compute Recall@{5, 10, 50, 100} on the full validation set of  $N = 1,564$  studies. Retrieval is based on cosine similarity in the shared image–text embedding space, and a query is counted as correct if the paired CT scan appears among the top- $K$  nearest neighbors.

Fig. 7 visualizes the joint embedding distribution of CT-RATE after UMAP projection, showing extensive cross-modal overlap and a smooth trajectory correlated with the total number of abnormalities described in the reports. This overlap indicates that the model learns a coherent shared latent space in which radiology images and their associated reports are embedded consistently, suggesting that the representations are largely modality-agnostic and capture clinically meaningful semantics rather than modality-specific artifacts. The continuous progression along the manifold with increasing abnormality count further supports the notion that the embedding space encodes a graded representation of pathology severity or complexity.

For MERLIN, we mirror the evaluation strategy presented in the original paper. Retrieval is conducted separately for the *Impressions* and the *Findings* sections, and performance is quantified using Recall@{1, 8}. Rather than the full test set, MERLIN evaluates retrieval over sampling pools of fixed sizes  $N \in \{32, 64, 128\}$ , each representing a different difficulty level. Cosine similarity is again used to rank image–text pairs, and correctness is assessed based on whether the paired CT volume is returned within the top- $K$  matches.

### C.4. Hardware

All downstream and ablation experiments are performed on a single H100 GPU (NVIDIA Corp., CA, USA) containing 96 GB of GPU memory, hosted in a system equipped with an AMD 4th Gen EPYC processor (18 cores, 36 threads) and 180 GB of system memory.

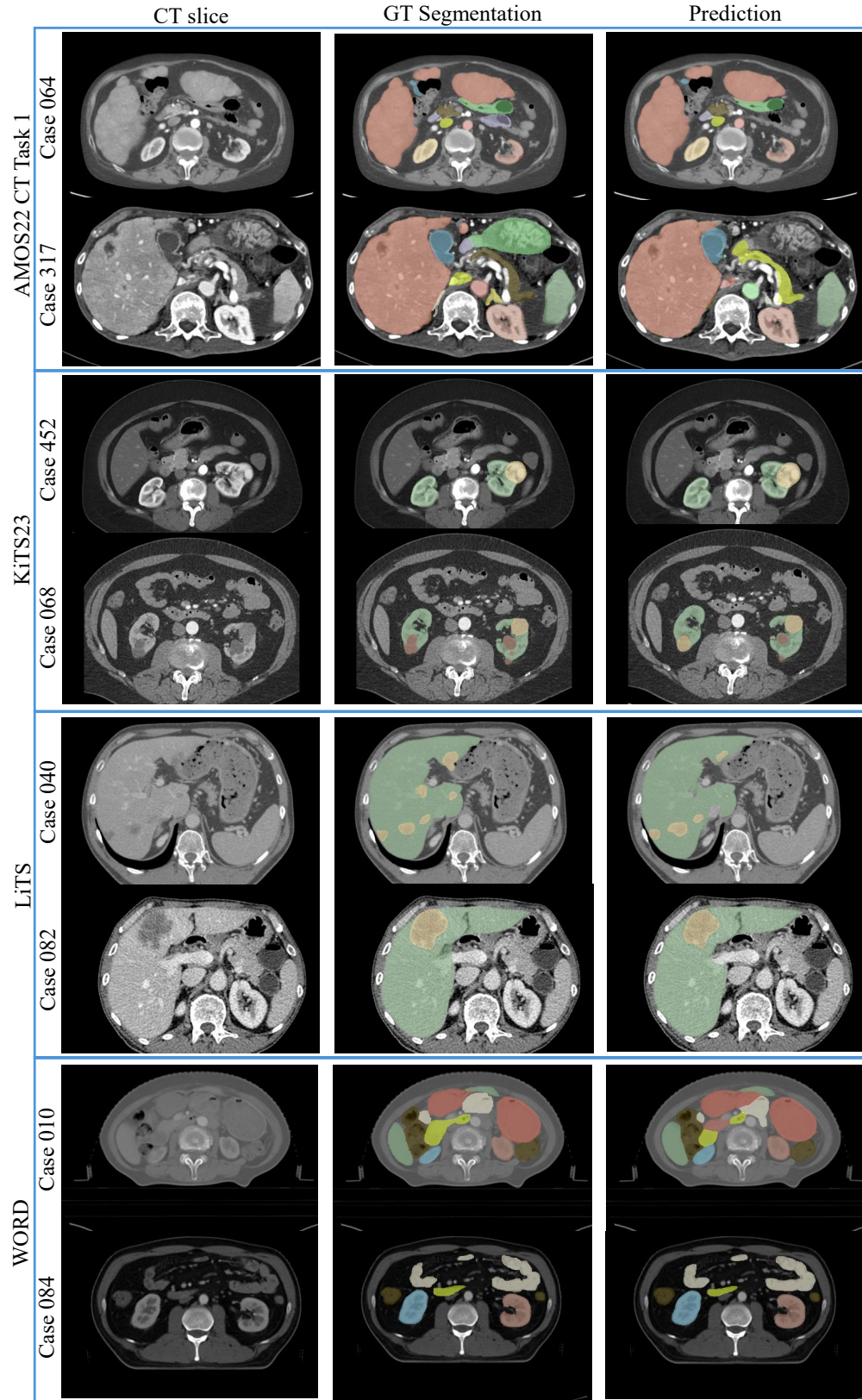


Figure 6. Curated example semantic segmentation predictions of SPECTRE on the different datasets employed in this work. Predictions with good performance and with the worst performance are depicted. Window settings optimized for organs of interest.

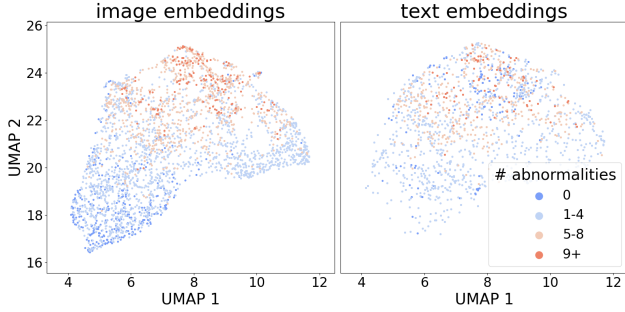


Figure 7. UMAP [42] visualization of image and text embeddings from the CT-RATE validation set [21]. Each point represents a sample categorized by the number of abnormalities noted in the corresponding radiology report.

## References

[1] Hugo J. W. L. Aerts, Emmanuel Rios Velazquez, Ralph T. H. Leijenaar, Chintan Parmar, Patrick Grossmann, Sara Carvalho, Johan Bussink, René Monshouwer, Benjamin Haibe-Kains, Derek Rietveld, Frank Hoebers, Michelle M. Rietbergen, C. René Leemans, Andre Dekker, John Quackenbush, Robert J. Gillies, and Philippe Lambin. Decoding tumour phenotype by noninvasive imaging using a quantitative radiomics approach. *Nature Communications*, 5(1):4006, 2014. [7](#), [3](#)

[2] Md Mahfuz Al Hasan, Mahdi Zaman, Abdul Jawad, Alberto Santamaría-Pang, Ho Hin Lee, Ivan Tarapov, Kyle B. See, Md Shah Imran, Antika Roy, Yaser Pourmohammadi Fal-lah, Navid Asadizanjan, and Reza Forghani. WaveFormer: A 3D Transformer with Wavelet-Driven Feature Representation for Efficient Medical Image Segmentation. In *Medical Image Computing and Computer Assisted Intervention – MICCAI 2025*, pages 684–694. 2026. [3](#), [7](#), [5](#)

[3] Natália Alves, Megan Schuurmans, Dawid Rutkowski, Derya Yakar, Ingfrid Haldorsen, Marjolein Liedenbaum, Anders Molven, Pierpaolo Vendittelli, Geert Litjens, John Hermans, and Henkjan Huisman. The PANORAMA Study Protocol: Pancreatic Cancer Diagnosis - Radiologists Meet AI. Technical report, Zenodo, 2024. [1](#), [2](#)

[4] Shaimaa Bakr, Olivier Gevaert, Sebastian Echegaray, Kelsey Ayers, Mu Zhou, Majid Shafiq, Hong Zheng, Jalen Anthony Benson, Weiruo Zhang, Ann N. C. Leung, Michael Kadoch, Chuong D. Hoang, Joseph Shrager, Andrew Quon, Daniel L. Rubin, Sylvia K. Plevritis, and Sandy Napel. A radiogenomic dataset of non-small cell lung cancer. *Scientific Data*, 5:180202, 2018. [7](#), [3](#)

[5] Shruthi Bannur, Stephanie Hyland, Qianchu Liu, Fernando Pérez-García, Maximilian Ilse, Daniel C. Castro, Benedikt Boecking, Harshita Sharma, Kenza Bouzid, Anja Thieme, Anton Schwaighofer, Maria Wetscherek, Matthew P. Lungen, Aditya Nori, Javier Alvarez-Valle, and Ozan Oktay. Learning To Exploit Temporal Structure for Biomedical Vision-Language Processing. In *Proceedings of the IEEE/CVF Conference on Computer Vision and Pattern Recognition*, pages 15016–15027, 2023. [2](#)

[6] Patrick Bilic, Patrick Christ, Hongwei Bran Li, Eugene Vorontsov, Avi Ben-Cohen, Georgios Kaassis, Adi Szeskin, Colin Jacobs, Gabriel Efrain Humpire Mamani, Gabriel Chartrand, Fabian Lohöfer, Julian Walter Holch, Wieland Sommer, Felix Hofmann, Alexandre Hostettler, Naama Lev-Cohain, Michal Drozdzał, Michal Marianne Amitai, Rafael Vivanti, Jacob Sosna, Ivan Ezhov, Anjany Sekuboyina, Fernando Navarro, Florian Kofler, Johannes C. Paetzold, Suprosanna Shit, Xiaobin Hu, Jana Lipková, Markus Rempfler, Marie Piraud, Jan Kirschke, Benedikt Wiestler, Zhiheng Zhang, Christian Hülsemeyer, Marcel Beetz, Florian Ettlinger, Michela Antonelli, Woong Bae, Míriam Bel-íver, Lei Bi, Hao Chen, Grzegorz Chlebus, Erik B. Dam, Qi Dou, Chi-Wing Fu, Bogdan Georgescu, Xavier Giró-i Nieto, Felix Gruen, Xu Han, Pheng-Ann Heng, Jürgen Hesser, Jan Hendrik Moltz, Christian Igel, Fabian Isensee, Paul Jäger, Fucang Jia, Krishna Chaitanya Kaluva, Mahendra Khened, Ildoo Kim, Jae-Hun Kim, Sungwoong Kim, Simon Kohl, Tomasz Konopczynski, Avinash Kori, Ganapathy Krishnamurthi, Fan Li, Hongchao Li, Junbo Li, Xiaomeng Li, John Lowengrub, Jun Ma, Klaus Maier-Hein, Kevins-Kokitsi Maninis, Hans Meine, Dorit Merhof, Akshay Pai, Mathias Perslev, Jens Petersen, Jordi Pont-Tuset, Jin Qi, Xiaojuan Qi, Oliver Rippel, Karsten Roth, Ignacio Sarasua, Andrea Schenk, Zengming Shen, Jordi Torres, Christian Wachinger, Chunliang Wang, Leon Weninger, Jianrong Wu, Daguang Xu, Xiaoping Yang, Simon Chun-Ho Yu, Yadong Yuan, Miao Yue, Liping Zhang, Jorge Cardoso, Spyridon Bakas, Rickmer Braren, Volker Heinemann, Christopher Pal, An Tang, Samuel Kadoury, Luc Soler, Bram van Ginneken, Hayit Greenspan, Leo Joskowicz, and Bjoern Menze. The Liver Tumor Segmentation Benchmark (LiTS). *Medical Image Analysis*, 84:102680, 2023. [7](#)

[7] Louis Blankemeier, Joseph Paul Cohen, Ashwin Kumar, Dave Van Veen, Syed Jamal Safdar Gardezi, Magdalini Paschali, Zhihong Chen, Jean-Benoit Delbrouck, Eduardo Reis, Cesar Truys, Christian Bluethgen, Malte Engmann Kjeldskov Jensen, Sophie Ostmeier, Maya Varma, Jeya Maria Jose Valanarasu, Zhongnan Fang, Zepeng Huo, Zaid Nabulsi, Diego Ardila, Wei-Hung Weng, Edson Amaro Junior, Neera Ahuja, Jason Fries, Nigam H. Shah, Andrew Johnston, Robert D. Boutin, Andrew Wentland, Curtis P. Langlotz, Jason Hom, Sergios Gatidis, and Akshay S. Chaudhari. Merlin: A Vision Language Foundation Model for 3D Computed Tomography, 2024. [3](#), [7](#), [8](#), [1](#)

[8] Tim G. W. Boers, Kiki N. Fockens, Joost A. van der Putten, Tim J. M. Jaspers, Carolus H. J. Kusters, Jelmer B. Jukema, Martijn R. Jong, Maarten R. Struyvenberg, Jeroen de Groof, Jacques J. Bergman, Peter H. N. de With, and Fons van der Sommen. Foundation models in gastrointestinal endoscopic AI: Impact of architecture, pre-training approach and data efficiency. *Medical Image Analysis*, 98:103298, 2024. [2](#)

[9] Mathilde Caron, Hugo Touvron, Ishan Misra, Hervé Jégou, Julien Mairal, Piotr Bojanowski, and Armand Joulin. Emerging Properties in Self-Supervised Vision Transformers. In *Proceedings of the IEEE/CVF International Conference on Computer Vision*, pages 9650–9660, 2021. [5](#)

[10] Richard J. Chen, Tong Ding, Ming Y. Lu, Drew F. K.

Williamson, Guillaume Jaume, Andrew H. Song, Bowen Chen, Andrew Zhang, Daniel Shao, Muhammad Shaban, Mane Williams, Lukas Oldenburg, Luca L. Weishaupt, Judy J. Wang, Anurag Vaidya, Long Phi Le, Georg Gerber, Sharifa Sahai, Walt Williams, and Faisal Mahmood. Towards a general-purpose foundation model for computational pathology. *Nature Medicine*, 30(3):850–862, 2024. 2

[11] Ting Chen, Simon Kornblith, Mohammad Norouzi, and Geoffrey Hinton. A simple framework for contrastive learning of visual representations. In *Proceedings of the 37th International Conference on Machine Learning*, pages 1597–1607, 2020. 1

[12] Mehdi Cherti, Romain Beaumont, Ross Wightman, Mitchell Wortsman, Gabriel Ilharco, Cade Gordon, Christoph Schuhmann, Ludwig Schmidt, and Jenia Jitsev. Reproducible Scaling Laws for Contrastive Language-Image Learning. In *Proceedings of the IEEE/CVF Conference on Computer Vision and Pattern Recognition*, pages 2818–2829, 2023. 8

[13] Noel C. F. Codella, Ying Jin, Shrey Jain, Yu Gu, Ho Hin Lee, Asma Ben Abacha, Alberto Santamaría-Pang, Will Guyman, Naiteek Sangani, Sheng Zhang, Hoifung Poon, Stephanie Hyland, Shruthi Bannur, Javier Alvarez-Valle, Xue Li, John Garrett, Alan McMillan, Gaurav Rajguru, Madhu Maddi, Nilesh Vijayrania, Rehaan Bhimai, Nick Mecklenburg, Rupal Jain, Daniel Holstein, Naveen Gaur, Vijay Aski, Jenq-Neng Hwang, Thomas Lin, Ivan Tarapov, Matthew Lungren, and Mu Wei. MedImageInsight: An Open-Source Embedding Model for General Domain Medical Imaging, 2024. 3

[14] Jia Deng, Wei Dong, Richard Socher, Li-Jia Li, Kai Li, and Li Fei-Fei. ImageNet: A large-scale hierarchical image database. In *Proceedings of the IEEE/CVF Conference on Computer Vision and Pattern Recognition*, pages 248–255, 2009. 3

[15] Alexey Dosovitskiy, Lucas Beyer, Alexander Kolesnikov, Dirk Weissenborn, Xiaohua Zhai, Thomas Unterthiner, Mostafa Dehghani, Matthias Minderer, Georg Heigold, Sylvain Gelly, Jakob Uszkoreit, and Neil Houlsby. An Image is Worth 16x16 Words: Transformers for Image Recognition at Scale. In *Proceedings of the International Conference on Learning Representations*, 2020. 2, 4

[16] Stéphane D’Ascoli, Hugo Touvron, Matthew L. Leavitt, Ari S. Morcos, Giulio Biroli, and Levent Sagun. ConViT: Improving Vision Transformers with Soft Convolutional Inductive Biases. In *Proceedings of the 38th International Conference on Machine Learning*, pages 2286–2296, 2021. 2

[17] Lijie Fan, Dilip Krishnan, Phillip Isola, Dina Katabi, and Yonglong Tian. Improving CLIP Training with Language Rewrites. In *Advances in Neural Information Processing Systems*, 2023. 2

[18] Cristhian Forigua, Maria Escobar, and Pablo Arbelaez. SuperFormer: Volumetric Transformer Architectures for MRI Super-Resolution. In *Simulation and Synthesis in Medical Imaging*, pages 132–141, 2022. 3

[19] Hadrien T. Gayap and Moulay A. Akhloufi. SALM: A Unified Model for 2D and 3D Region of Interest Segmentation in Lung CT Scans Using Vision Transformers. *Applied Bio-sciences*, 4(1):11, 2025. 2

[20] Jean-Bastien Grill, Florian Strub, Florent Altché, Corentin Tallec, Pierre H. Richemond, Elena Buchatskaya, Carl Doersch, Bernardo Avila Pires, Zhaohan Daniel Guo, Mohammad Gheshlaghi Azar, Bilal Piot, Koray Kavukcuoglu, Rémi Munos, and Michal Valko. Bootstrap your own latent a new approach to self-supervised learning. In *Proceedings of the 34th International Conference on Neural Information Processing Systems*, pages 21271–21284, 2020. 1

[21] Ibrahim Ethem Hamamci, Sezgin Er, Furkan Almas, Ayse Gulnihan Simsek, Seval Nil Esirgun, Irem Dogan, Muhammed Furkan Dasdelen, Bastian Wittmann, Enis Simsar, Mehmet Simsar, Emine Bensu Erdemir, Abdullah Alanbay, Anjany Sekuboyina, Berkcan Lafci, Mehmet K. Ozdemir, and Bjoern Menze. A foundation model utilizing chest CT volumes and radiology reports for supervised-level zero-shot detection of abnormalities, 2024. 2, 3, 7, 8, 1, 9

[22] Ali Hatamizadeh, Vishwesh Nath, Yucheng Tang, Dong Yang, Holger R. Roth, and Daguang Xu. Swin UNETR: Swin Transformers for Semantic Segmentation of Brain Tumors in MRI Images. In *Brainlesion: Glioma, Multiple Sclerosis, Stroke and Traumatic Brain Injuries*, pages 272–284, 2022. 2

[23] Ali Hatamizadeh, Yucheng Tang, Vishwesh Nath, Dong Yang, Andriy Myronenko, Bennett Landman, Holger R. Roth, and Daguang Xu. UNETR: Transformers for 3D Medical Image Segmentation. In *Proceedings of the IEEE/CVF Winter Conference on Applications of Computer Vision*, pages 574–584, 2022. 2, 7, 5

[24] Kaiming He, Xinlei Chen, Saining Xie, Yanghao Li, Piotr Dollár, and Ross Girshick. Masked Autoencoders Are Scalable Vision Learners. In *Proceedings of the IEEE/CVF Conference on Computer Vision and Pattern Recognition*, pages 16000–16009, 2022. 5

[25] Yufan He, Vishwesh Nath, Dong Yang, Yucheng Tang, Andriy Myronenko, and Daguang Xu. SwinUNETR-V2: Stronger Swin Transformers with Stagewise Convolutions for 3D Medical Image Segmentation. In *Medical Image Computing and Computer Assisted Intervention – MICCAI 2023*, pages 416–426, 2023. 2, 7, 5

[26] Yufan He, Pengfei Guo, Yucheng Tang, Andriy Myronenko, Vishwesh Nath, Ziyue Xu, Dong Yang, Can Zhao, Benjamin Simon, Mason Belue, Stephanie Harmon, Baris Turkbey, Daguang Xu, and Wenqi Li. VISTA3D: A Unified Segmentation Foundation Model For 3D Medical Imaging. In *Proceedings of the IEEE/CVF Conference on Computer Vision and Pattern Recognition*, pages 20863–20873, 2025. 3

[27] Nicholas Heller, Fabian Isensee, Klaus H. Maier-Hein, Xiaoshuai Hou, Chunmei Xie, Fengyi Li, Yang Nan, Guangrui Mu, Zhiyong Lin, Miofei Han, Guang Yao, Yaozong Gao, Yao Zhang, Yixin Wang, Feng Hou, Jiawei Yang, Guangwei Xiong, Jiang Tian, Cheng Zhong, Jun Ma, Jack Rickman, Joshua Dean, Bethany Stai, Resha Tejpaul, Makinna Oestreich, Paul Blake, Heather Kaluzniak, Shaneabbas Raza, Joel Rosenberg, Keenan Moore, Edward Walczak, Zachary Rengel, Zach Edgerton, Ranveer Vasdev, Matthew Peterson, Sean McSweeney, Sarah Peterson, Arveen Kalapara, Niranjan Sathianathan, Nikolaos Papanikolopoulos, and Christopher Weight. The state of the art in kidney and kidney tumor

segmentation in contrast-enhanced CT imaging: Results of the KiTS19 challenge. *Medical Image Analysis*, 67:101821, 2021. 7, 3

[28] Shih-Cheng Huang, Zepeng Huo, Ethan Steinberg, Chia-Chun Chiang, Curtis Langlotz, Matthew Lungren, Serena Yeung, Nigam Shah, and Jason Fries. INSPECT: A Multi-modal Dataset for Patient Outcome Prediction of Pulmonary Embolisms. *Advances in Neural Information Processing Systems*, 36:17742–17772, 2023. 1

[29] Fabian Isensee, Paul F. Jaeger, Simon A. A. Kohl, Jens Petersen, and Klaus H. Maier-Hein. nnU-Net: a self-configuring method for deep learning-based biomedical image segmentation. *Nature Methods*, 18(2):203–211, 2021. 7, 5

[30] Fabian Isensee, Tassilo Wald, Constantin Ulrich, Michael Baumgartner, Saikat Roy, Klaus Maier-Hein, and Paul F. Jäger. nnU-Net Revisited: A Call for Rigorous Validation in 3D Medical Image Segmentation. In *Medical Image Computing and Computer Assisted Intervention – MICCAI 2024*, pages 488–498. 2024. 7, 4, 5

[31] Tim Jaspers, Ronald De Jong, Yiping Li, Carolus H J Kusters, Franciscus H A Bakker, Romy C. Van Jaarsveld, Gino M. Kuiper, Richard Van Hillegersberg, Jelle P. Ruurda, Willem M. Brinkman, Josien P W Pluim, Peter H N De With, Marcel Breeuwer, Yasmina Al Khalil, and Fons Van Der Sommen. Scaling up self-supervised learning for improved surgical foundation models. *Medical Image Analysis*, page 103873, 2025. 2

[32] Yuanfeng Ji, Haotian Bai, Chongjian Ge, Jie Yang, Ye Zhu, Ruimao Zhang, Zhen Li, Lingyan Zhanng, Wanling Ma, Xiang Wan, and Ping Luo. AMOS: A Large-Scale Abdominal Multi-Organ Benchmark for Versatile Medical Image Segmentation. In *Advances in Neural Information Processing Systems*, 2022. 7, 1, 2, 5

[33] Feyza Duman Keles, Pruthuvi Mahesakya Wijewardena, and Chinmay Hegde. On The Computational Complexity of Self-Attention. In *Proceedings of the 34th International Conference on Algorithmic Learning Theory*, 2022. 2

[34] Tommie Kerssies, Niccolò Cavagnero, Alexander Hermans, Narges Norouzi, Giuseppe Averta, Bastian Leibe, Gijs Dubbelman, and Daan de Geus. Your ViT is Secretly an Image Segmentation Model. In *Proceedings of the IEEE/CVF Conference on Computer Vision and Pattern Recognition*, pages 25303–25313, 2025. 7, 4

[35] Wenhui Lei, Hanyu Chen, Zitian Zhang, Luyang Luo, Qiong Xiao, Yannian Gu, Peng Gao, Yankai Jiang, Ci Wang, Guangtao Wu, Tongjia Xu, Yingjie Zhang, Pranav Rajpurkar, Xiaofan Zhang, Shaoting Zhang, and Zhenning Wang. A Synthetic Data-Driven Radiology Foundation Model for Pan-tumor Clinical Diagnosis, 2025. 4, 3

[36] Wenxuan Li, Chongyu Qu, Xiaoxi Chen, Pedro R. A. S. Bassi, Yijia Shi, Yuxiang Lai, Qian Yu, Huimin Xue, Yixiong Chen, Xiaorui Lin, Yutong Tang, Yining Cao, Haoqi Han, Zheyuan Zhang, Jiawei Liu, Tiezheng Zhang, Yujiu Ma, Jincheng Wang, Guang Zhang, Alan Yuille, and Zongwei Zhou. AbdomenAtlas: A large-scale, detailed-annotated, & multi-center dataset for efficient transfer learning and open algorithmic benchmarking. *Medical Image Analysis*, 97:103285, 2024. 3, 1

[37] Wenxuan Li, Alan Yuille, and Zongwei Zhou. How Well Do Supervised 3D Models Transfer to Medical Imaging Tasks?, 2025. 3

[38] Ze Liu, Yutong Lin, Yue Cao, Han Hu, Yixuan Wei, Zheng Zhang, Stephen Lin, and Baining Guo. Swin Transformer: Hierarchical Vision Transformer using Shifted Windows. In *Proceedings of the IEEE/CVF International Conference on Computer Vision*, pages 9992–10002, 2021. 3

[39] Ilya Loshchilov and Frank Hutter. Decoupled Weight Decay Regularization. In *Proceedings of the International Conference on Learning Representations*, 2018. 5

[40] Xiangde Luo, Wenjun Liao, Jianghong Xiao, Jieneng Chen, Tao Song, Xiaofan Zhang, Kang Li, Dimitris N. Metaxas, Guotai Wang, and Shaoting Zhang. WORD: A large scale dataset, benchmark and clinical applicable study for abdominal organ segmentation from CT image. *Medical Image Analysis*, 82:102642, 2022. 7

[41] Jun Ma, Yao Zhang, Song Gu, Cheng Zhu, Cheng Ge, Yichi Zhang, Xingle An, Congcong Wang, Qiyuan Wang, Xin Liu, Shucheng Cao, Qi Zhang, Shangqing Liu, Yunpeng Wang, Yuhui Li, Jian He, and Xiaoping Yang. AbdomenCT-1K: Is Abdominal Organ Segmentation a Solved Problem? *IEEE Transactions on Pattern Analysis and Machine Intelligence*, 44(10):6695–6714, 2022. 1, 2

[42] Leland McInnes, John Healy, Nathaniel Saul, and Lukas Großberger. UMAP: Uniform Manifold Approximation and Projection. *Journal of Open Source Software*, 3(29):861, 2018. 9

[43] Aaron van den Oord, Yazhe Li, and Oriol Vinyals. Representation Learning with Contrastive Predictive Coding, 2019. 6

[44] Maxime Oquab, Timothée Darcet, Théo Moutakanni, Huy V. Vo, Marc Szafraniec, Vasil Khalidov, Pierre Fernandez, Daniel Haziza, Francisco Massa, Alaaeldin El-Nouby, Mido Assran, Nicolas Ballas, Wojciech Galuba, Russell Howes, Po-Yao Huang, Shang-Wen Li, Ishan Misra, Michael Rabat, Vasu Sharma, Gabriel Synnaeve, Hu Xu, Herve Jegou, Julien Mairal, Patrick Labatut, Armand Joulin, and Piotr Bojanowski. DINOv2: Learning Robust Visual Features without Supervision. *Transactions on Machine Learning Research*, 2023. 5

[45] Suraj Pai, Dennis Bontempi, Ibrahim Hadzic, Vasco Prudente, Mateo Sokač, Tafadzwa L. Chaunzwa, Simon Bernatz, Ahmed Hosny, Raymond H. Mak, Nicolai J. Birkbak, and Hugo J. W. L. Aerts. Foundation model for cancer imaging biomarkers. *Nature Machine Intelligence*, pages 1–14, 2024. 3

[46] Suraj Pai, Ibrahim Hadzic, Dennis Bontempi, Keno Bressem, Benjamin H. Kann, Andriy Fedorov, Raymond H. Mak, and Hugo J. W. L. Aerts. Vision Foundation Models for Computed Tomography, 2025. 3

[47] Suraj Pai, Ibrahim Hadzic, Andrey Fedorov, Raymond H. Mak, and Hugo JW Aerts. Foundation model embeddings for quantitative tumor imaging biomarkers, 2025. 6, 3, 4

[48] Alec Radford, Jong Wook Kim, Chris Hallacy, Aditya Ramesh, Gabriel Goh, Sandhini Agarwal, Girish Sastry,

Amanda Askell, Pamela Mishkin, and Jack Clark. Learning transferable visual models from natural language supervision. In *International conference on machine learning*, pages 8748–8763, 2021. 1, 3, 6

[49] Alexandre Sablayrolles, Matthijs Douze, Cordelia Schmid, and Hervé Jégou. Spreading vectors for similarity search. In *Proceedings of the International Conference on Learning Representations*, 2018. 5

[50] Arnaud Arindra Adiyoso Setio, Alberto Traverso, Thomas de Bel, Moira S. N. Berens, Cas van den Bogaard, Piergiorgio Cerello, Hao Chen, Qi Dou, Maria Evelina Fantacci, Bram Geurts, Robbert van der Gugten, Pheng Ann Heng, Bart Jansen, Michael M. J. de Kaste, Valentin Kotov, Jack Yu-Hung Lin, Jeroen T. M. C. Manders, Alexander Sóniora-Mengana, Juan Carlos García-Naranjo, Evgenia Papavasileiou, Mathias Prokop, Marco Saletta, Cornelia M Schaefer-Prokop, Ernst T. Scholten, Luuk Scholten, Miranda M. Snoeren, Ernesto Lopez Torres, Jef Vandemeulebroucke, Nicole Walasek, Guido C. A. Zuidhof, Bram van Ginneken, and Colin Jacobs. Validation, comparison, and combination of algorithms for automatic detection of pulmonary nodules in computed tomography images: The LUNA16 challenge. *Medical Image Analysis*, 42:1–13, 2017. 7, 3

[51] Amber L. Simpson, Jacob Peoples, John M. Creasy, Gabor Fichtinger, Natalie Gangai, Krishna N. Keshavamurthy, Andras Lasso, Jinru Shia, Michael I. D’Angelica, and Richard K. G. Do. Preoperative CT and survival data for patients undergoing resection of colorectal liver metastases. *Scientific Data*, 11(1):172, 2024. 7, 3, 4

[52] Oriane Siméoni, Huy V. Vo, Maximilian Seitzer, Federico Baldassarre, Maxime Oquab, Cijo Jose, Vasil Khalidov, Marc Szafraniec, Seungeun Yi, Michaël Ramamonjisoa, Francisco Massa, Daniel Haziza, Luca Wehrstedt, Jianyuan Wang, Timothée Darcet, Théo Moutakanni, Leonel Sentana, Claire Roberts, Andrea Vedaldi, Jamie Tolan, John Brandt, Camille Couprie, Julien Mairal, Hervé Jégou, Patrick Labatut, and Piotr Bojanowski. DINOv3, 2025. 3, 5

[53] Jianlin Su, Murtadha Ahmed, Yu Lu, Shengfeng Pan, Wen Bo, and Yunfeng Liu. RoFormer: Enhanced transformer with Rotary Position Embedding. *Neurocomputing*, 568:127063, 2024. 5

[54] The NLST Research Team. Reduced Lung-Cancer Mortality with Low-Dose Computed Tomographic Screening. *New England Journal of Medicine*, 365(5):395–409, 2011. 1

[55] Tassilo Wald, Saikat Roy, Fabian Isensee, Constantin Ulrich, Sebastian Ziegler, Dasha Trofimova, Raphael Stock, Michael Baumgartner, Gregor Köhler, and Klaus H. Maier-Hein. Primus: Enforcing Attention Usage for 3D Medical Image Segmentation. *CoRR*, 2025. 2, 7, 5

[56] Tassilo Wald, Constantin Ulrich, Jonathan Suprijadi, Sebastian Ziegler, Michal Nohel, Robin Peretzke, Gregor Kohler, and Klaus Maier-Hein. An OpenMind for 3D Medical Vision Self-supervised Learning. In *Proceedings of the IEEE/CVF International Conference on Computer Vision*, pages 23839–23879, 2025. 4

[57] Avivah J. Wang, Fakrul Islam Tushar, Michael R. Harowicz, Betty C. Tong, Kyle J. Lafata, Tina D. Tailor, and Joseph Y. Lo. The Duke Lung Cancer Screening (DLCS) Dataset: A Reference Dataset of Annotated Low-Dose Screening Thoracic CT. *Radiology: Artificial Intelligence*, 7(4):e240248, 2025. 7, 3

[58] Jakob Wasserthal, Hanns-Christian Breit, Manfred T. Meyer, Maurice Pradella, Daniel Hinck, Alexander W. Sauter, Tobias Heye, Daniel T. Boll, Joshy Cyriac, Shan Yang, Michael Bach, and Martin Segeroth. TotalSegmentator: Robust Segmentation of 104 Anatomic Structures in CT Images. *Radiology: Artificial Intelligence*, 5(5):e230024, 2023. 1

[59] Linshan Wu, Jiaxin Zhuang, and Hao Chen. VoCo: A Simple-yet-Effective Volume Contrastive Learning Framework for 3D Medical Image Analysis. In *Proceedings of the IEEE/CVF Conference on Computer Vision and Pattern Recognition*, pages 22873–22882, 2024. 3

[60] Yutong Xie, Jianpeng Zhang, Chunhua Shen, and Yong Xia. CoTr: Efficiently Bridging CNN and Transformer for 3D Medical Image Segmentation. In *Medical Image Computing and Computer Assisted Intervention – MICCAI 2021*, pages 171–180. 2021. 7, 5

[61] Xiaohua Zhai, Basil Mustafa, Alexander Kolesnikov, and Lucas Beyer. Sigmoid Loss for Language Image Pre-Training. In *Proceedings of the IEEE/CVF International Conference on Computer Vision*, pages 11975–11986, 2023. 6

[62] Sheng Zhang, Yanbo Xu, Naoto Usuyama, Hanwen Xu, Jaspreet Bagga, Robert Tinn, Sam Preston, Rajesh Rao, Mu Wei, Naveen Valluri, Cliff Wong, Andrea Tupini, Yu Wang, Matt Mazzola, Swadheen Shukla, Lars Liden, Jianfeng Gao, Angela Crabtree, Brian Piening, Carlo Bifulco, Matthew P. Lungren, Tristan Naumann, Sheng Wang, and Hoifung Poon. BiomedCLIP: a multimodal biomedical foundation model pretrained from fifteen million scientific image-text pairs, 2025. 8

[63] Yanzhao Zhang, Mingxin Li, Dingkun Long, Xin Zhang, Huan Lin, Baosong Yang, Pengjun Xie, An Yang, Dayiheng Liu, Junyang Lin, Fei Huang, and Jingren Zhou. Qwen3 Embedding: Advancing Text Embedding and Reranking Through Foundation Models, 2025. 6

[64] Hong-Yu Zhou, Jiansen Guo, Yinghao Zhang, Xiaoguang Han, Lequan Yu, Liansheng Wang, and Yizhou Yu. nnFormer: Volumetric Medical Image Segmentation via a 3D Transformer. *IEEE Transactions on Image Processing*, 32: 4036–4045, 2023. 2, 7, 5

[65] Jinghao Zhou, Chen Wei, Huiyu Wang, Wei Shen, Cihang Xie, Alan Yuille, and Tao Kong. Image BERT Pre-training with Online Tokenizer. In *Proceedings of the International Conference on Learning Representations*, 2021. 5

[66] Zongwei Zhou, Vatsal Sodha, Jiaxuan Pang, Michael B. Gotway, and Jianming Liang. Models Genesis. *Medical Image Analysis*, 67:101840, 2021. 4, 3